1 **Spatial distribution of aerosol microphysical and optical properties and**

2 **direct radiative effect from the China Aerosol Remote Sensing Network**

3 Huizheng Che[1][*], Xiangao Xia[2,3], Hujia Zhao[1,4], Oleg Dubovik[5], Brent N.

4 Holben[6], Philippe Goloub[5], Emilio Cuevas-Agulló[7], Victor Estelles[8], Yaqiang

5 Wang[1], Jun Zhu[9] Bing Qi[10], Wei Gong [11], Honglong Yang[12], Renjian Zhang[13],

6 Leiku Yang[14], Jing Chen[15], Hong Wang[1], Yu Zheng[1], Ke Gui[1,2],Xiaochun

7 Zhang[16], Xiaoye Zhang[1][*]

8 1 State Key Laboratory of Severe Weather (LASW) and Key Laboratory of Atmospheric
9   Chemistry (LAC), Chinese Academy of Meteorological Sciences, CMA, Beijing,
10   100081, China

11 2 Laboratory for Middle Atmosphere and Global Environment Observation (LAGEO),
12   Institute of Atmospheric Physics, Chinese Academy of Sciences, Beijing, 100029,
13   China

14 3 University of Chinese Academy of Science, Beijing, 100049, China

15 4 Institute of Atmospheric Environment, CMA, Shenyang, 110016, China

16 5 Laboratoire d'Optique Amosphérique, Université des Sciences et Technologies de
17   Lille, 59655, Villeneuve d'Ascq, France

18 6 NASA Goddard Space Flight Center, Greenbelt, MD, USA

19 7 Centro de Investigación Atmosférica de Izaña, AEMET, 38001 Santa Cruz de
20   Tenerife , Spain

21 8 Dept. Fisica de la Terra i Termodinamica, Universitat de Valencia, C/ Dr. Moliner 50,
22   46100 Burjassot, Spain

23 9 Collaborative Innovation Center on Forecast and Evaluation of Meteorological
24   Disasters, Nanjing University of Information Science & Technology, Nanjing, 210044,
25   China

26 10 Hangzhou Meteorological Bureau, Hangzhou, 310051, China

27 11 State Key Laboratory of Information Engineering in Surveying, Mapping and Remote
28   Sensing, Wuhan University, Wuhan, 430079, China

29 12 Shenzhen Meteorological Bureau, Shenzhen, 518040, China

30 13 Key Laboratory of Regional Climate-Environment Research for Temperate East Asia,
31   Institute of Atmospheric Physics, Beijing, 100029, Chinese Academy of Sciences.

32 14 School of Surveying and Land Information Engineering, Henan Polytechnic University,
33   Jiaozuo, 454000, China

34 15 Shijiazhuang Meteorological Bureau, Shijiazhuang, 050081, China

35 16 Meteorological Observation Center, CMA, Beijing, 100081

36 Corresponding author: chehz@cma.gov.cn & xiaoye@cma.gov.cn

Abstract

Long-term observations of aerosol microphysical and optical properties obtained through ground-based remote sensing at 50 China Aerosol Remote Sensing Network (CARSNET) sites were used to characterize the aerosol climatology for representative remote, rural, and urban areas over China to assess effects on climate. The annual mean effective radii for total particles (R_{efft}) decreased from north to south and from rural to urban sites, and high total particle volumes were found at the urban sites. The aerosol optical depth at 440 nm (AOD_{440nm}) increased from remote/rural sites (0.12) to urban sites (0.79), and the extinction Ångström exponent ($EAE_{440-870nm}$) increased from 0.71 at the arid/semi-arid sites to 1.15 at the urban sites, presumably due to anthropogenic emissions. Single scattering albedos ($SSA_{440\ nm}$) ranged from 0.88 to 0.92 indicating slightly to strongly absorbing aerosols. Absorption AOD_{440nm}'s were 0.01 at the remote sites versus 0.07 at the urban sites. The average direct aerosol radiative effect (DARE) at the bottom of atmosphere increased from the sites in the remote (-24.40 W/m^2) to the urban area (-103.28 W/m^2) indicating increased cooling at the latter. The DARE for the top of the atmosphere increased from -4.79 W/m^2 at the remote sites to -30.05 W/m^2 at the urban sites, indicating overall cooling effects for the earth-atmosphere system. A classification method based on $SSA_{440\ nm}$, fine mode fraction (FMF), and $EAE_{440-870\ nm}$ showed that coarse mode particles (mainly dust) were dominant at the rural sites near the northwestern deserts, while light-absorbing, fine-mode particles were important at most urban sites. This study will be useful for understanding aerosol climate effects and regional environmental pollution, and the results will provide useful information for satellite validation and the improvement of climate modelings.

Keywords: aerosol optical properties; direct aerosol radiative effect; aerosol type; climatology; China Aerosol Remote Sensing Network

1. Introduction

Atmospheric aerosols have important direct effects on climate because they can scatter and absorb radiant energy and in so doing affect the Earth's energy balance (Charlson et al., 1992). The optical properties of the aerosol determine the particles' direct effects on the Earth's radiative balance and climate change (Ramanathan et al., 2001; Eck et al., 2005; Myhre, 2009). Aerosol optical depth (AOD) is one of the key measures of the aerosols' effects on climate (Breon et al., 2002), and the extinction Ångström exponent (EAE) can be used together with AOD to study aerosol sizes and types (Gobbi et al., 2007; Eck et al., 1999). The aerosols' absorptivity is a key determinant of radiative effect (Haywood and Shine, 1995), and the single scattering albedo (SSA) is the parameter needed to calculate the direct aerosol radiative effect (Jacobson et al., 2000; Dubovik et al., 2002; Gelencser et al., 2004; Russell et al., 2010; Giles et al., 2012).

With the recognition of the importance for climate, the aerosol optical properties have been obtained from ground-based monitoring networks worldwide; some of the major networks include AERONET-Aerosol Robotic Network) (Holben et al., 1998) and its sub-networks of PHOTONS-PHOtométrie pour le Traitement Opérationnel de Normalisation Satellitaire, AEROCAN-Canadian Sun-Photometer Network, and RIMA-Iberian Network for aerosol measurements ((Goloub et al., 2007; Bokoye et al., 2001; Prats et al., 2011), SKYNET-SKYrad Network (Takamura and Nakajima, 2004; Che et al., 2008), EARLINET-European aerosol Lidar network (Pappalardo et al., 2014), the GAW-PFR Network-Global Atmosphere Watch Programmer-Precision Filter Radiometers (Wehrli, 2002; Estellés et al., 2012),. The CARSNET-China Aerosol Remote Sensing NETwork, the CSHNET-Chinese Sun Hazemeter Network and the SONET-Sun–Sky Radiometer Observation Network have been established to measure aerosol optical properties in China (Che et al., 2009a, 2015; Xin et al., 2007; Li et al., 2018). Furthermore, the aerosol optical properties have also been used in

96 comprehensive studies of aerosol physical characteristics and chemical

97 composition.

98   China has become one of the largest aerosol sources in the world due to

99 its rapid economic development, and this has caused significant effects on

100 local environments and regional climate (Che et al., 2005; Xia, 2010). There

101 have been numerous studies that have focused on aerosol optical properties

102 obtained though ground-based remote sensing methods in China (Luo et al.,

103 2002; Li et al., 2003; Duan and Mao, 2007). A few researches have pay more

104 attention to the aerosol optical properties and its radiative effects over the

105 urban-industrial areas as well as at coastal sites in northeastern China (Wang

106 et al., 2010; Xin et al., 2011; Xia et al., 2007; Zhao et al., 2016; Wu et al. 2012).

107 Many studies of aerosol optical properties conducted in northern China with

108 high aerosol loadings, such as the Beijing-Tianjin-Hebei region (Che et al.

109 2014; Xia et al., 2013; Fan et al., 2006; Xie et al., 2008). Aerosol optical

110 properties also have been investigated at Hefei, Shouxian, Nanjing, Taihu and

111 Shanghai in eastern China (Lee et al., 2010; He et al., 2012; Zhuang et al.,

112 2014; Wang Z et al., 2015; Che et al., 2018). Some studies of aerosol optical

113 properties have been made in southern China (Wang et al., 2015; Tao et al.,

114 2014), and those at remote and rural sites in China provide information on

115 regional background conditions (Che et al., 2009b; Wang et al., 2010; Xue et

116 al., 2011; Zhu et al., 2014; Yuan et al., 2014).

117   China's vast size, varied terrain, and heterogeneity of aerosol sources,

118 has led to strong temporal and spatial variability in aerosol optical and physical

119 properties. The mixtures of aerosol types at most sites are complex, and

120 aerosol populations' size and composition are affected by their sources,

121 transformations that occurring during transportation and removing processes

122 (Cao et al., 2007; Wang et al., 2007; Zhang et al., 2013; Wan et al., 2015).

123 National scale, ground-based measurements of aerosol microphysical and its

124 optical properties obtained from the sunphotometer provide for a better

125 understanding of the aerosols' climate effects over the different regions of

China. The measurements of greatest interest include aerosol size distributions, optical properties (AOD, AE, SSA, absorption AOD) because those data can be used to evaluate direct radiative effect.

The aim of this study was focused on the investigation of the climatological spatial distribution of aerosol microphysical and optical properties over regional-scales using spatial distribution data from the national CARSNET network. The data were collected at CARSNET sites, which include sites in the remote, rural and urban area, with the same calibration procedures and calculation algorithms were used at all sites. As a result, the data are directly comparable among sites (Che et al., 2009a), and the results can be provide to characterize the regional distribution and temporal variation of aerosol optical properties. This research focused on aerosol climate effects and regional environmental pollution, and the results should be useful for satellite validations and for the improvement of models in the future. The remainder of this paper is organized as following: Section 2 firstly describes the sites in detail, and then introduced the methods in data processing of the aerosol optical properties as well as the direct aerosol radiative effect calculation through the retrieved aerosol optical parameters. Section 3 illustrates the aerosol microphysical and optical properties, as well as its direct aerosol radiative effect. An aerosol type classification method is proposed according to the aerosol optical parameters. Section 4 presents the conclusions of the study.

2 Site description, instruments, and data

2.1 Site description

Sunphotometers (CE-318, Cimel Electronique, Paris, France, see Appendix A,) were installed at 50 CARSNET sites (Fig. 1) in multi-year from 2010 to 2017. The stations were classified as remote, rural, or urban sites based on administrative division (Appendix Table 1). Three of the remote stations were about more than 3000 m above the sea level on the Tibetan Plateau far from the anthropogenic influences, and one of them was a

northwestern regional background site in China. The 23 rural sites represent (a) five sites of desert regions (five sites) affected by most of dust aerosols rather than anthropogenic particles, (b) two sites affected by both dust and anthropogenic activities on the Loess Plateau, and (c) 16 sites located near or surrounding the large cities relatively strong to the impacts of anthropogenic activities in the central and eastern China. The last category is 24 urban sites located in provincial capitals or heavily populated cities.

2.2 Instruments and calibration

The CE-318 sunphotometers used in this study were calibrated annually, using the CARSNET calibration protocol, to verify the accuracy and reliability of the sky irradiance measurements (Holben et al., 1998; Che et al., 2009; Tao et al., 2014). The reference instruments for CARSNET were periodically calibrated at Izaña, Tenerife, Spain located at 28.31 °N, 16.50 °W (2391.0 m a.s.l.) in conjunction with the AERONET program. There is several different types of the Cimel instruments have been used of the 50 sites in this network as follows: (1) logical type CE-318 sunphotometers (440 nm, 675 nm, 870 nm, 940 nm, 1020 nm and three 870 nm at the polarization band), (2) numerical type CE-318 sunphotometers (440 nm, 675 nm, 870 nm, 940 nm, 1020 nm and three polarization bands at 870 nm), (3) numerical type CE-318 sunphotometers at eight wavelengths (340 nm, 380 nm, 440 nm, 500 nm, 675 nm, 870 nm, 940 nm, and 1020 nm), (4) and numerical type CE-318 sunphotometers at nine wavelengths (340 nm, 380 nm, 440 nm, 500 nm, 675 nm, 870 nm, 940 nm, 1020 nm and 1640 nm).

Measurements used to retrieve AODs were at 340 nm, 380 nm, 440 nm, 500 nm, 675 nm, 870 nm, 1020 nm, and 1640 nm, while the total precipitable water content was obtained by using those measurements at 940 nm (Holben et al., 1998; Dubovik and King, 2000). The cloud-screened AOD data were calculated by using the ASTPwin software, and extinction Ångström exponents (EAE) were calculated from the instantaneous AODs for wavelengths of 440 nm and 870 nm (Che et al., 2009, 2015). Sites with more than three daily AOD

186 observations and more than 10 monthly AOD observation days were used to

187 calculate the daily and monthly mean AODs and extinction Ångström

188 exponents. The FMF is described as the fraction of fine mode particles of total

189 AOD_{440nm} ($AOD_{fine440\ nm}/AOD_{440\ nm}$).

190

191 **2.3. Data processing**

192   The aerosol microphysical and optical properties, including volume size

193 distributions (dV(r)/dln(r), the total, fine, and coarse mode aerosol effective

194 radii (R_{effT}, R_{effF}, and R_{effC}, respectively) single-scattering albedo (SSA),

195 complex refractive indices, absorption AODs (AAODs), and absorption

196 Angström exponents (AAEs), were retrieved from the observational data from

197 the sky scattering channel of the sunphotometers at 440 nm, 670 nm, 870 nm,

198 1020 nm using the algorithms of Dubovik et al. (2002, 2006). In the process of

199 retrieval, the data of surface albedo (SA) was interpolated or extrapolated to

200 440 nm, 670 nm, 870 nm, and 1020 nm based on the daily MCD43C3 data, a

201 product from the MODIS-Moderate Resolution Imaging Spectroradiometer

202 surface reflectance (https://ladsweb.modaps.eosdis.nasa.gov/). The algorithm

203 used to calculate aerosol volume size distributions ($dV/\ln r$) was under the

204 assumption of a homogeneous distribution of non-spherical particles following

205 the approach of Dubovik (2006). The sphericity fraction retrieved from the

206 inversions is defined as: spherical particles/(spheroidal particles + spherical

207 particles) (Giles et al., 2011).

208   As Dubovik et al. (2002, 2006) defined that all the particles with effective

209 radii < 0.992 µm were considered as fine mode particles; and those > 0.992

210 µm were considered as coarse mode particles. For the total (R_{effT}), fine (R_{effF})

211 and coarse (R_{effC}) mode aerosols, the effective radii are calculated by the

212 equation as follows:

213 $$R_{eff} = \frac{\int_{r_{min}}^{r_{max}} r^3 \frac{dN(r)}{dlnr} dlnr}{\int_{r_{min}}^{r_{max}} r^2 \frac{dN(r)}{dlnr} dlnr} \qquad (1)$$

214   Where r_{min} denotes 0.05, 0.05, 0.992 μm and r_{max} denotes 15, 0.992, 15

215   μm of the total, fine and coarse mode particles, respectively.

216   The coarse (PVC) and fine aerosol particle volumes distributions (PVF)

217   are calculated according to a bimodal lognormal function descript by Whitby

218   (1978), Shettle and Fenn (1979) and Remer and Kaufman (1998):

219
$$\frac{dV(r)}{d\ln r} = \sum_{i=1}^{2} \frac{C_{v,i}}{\sqrt{2\pi}\sigma_i} exp\left[-\frac{(\ln r - \ln r_{V,i})^2}{2\sigma_i^2}\right] \tag{2}$$

220   where $C_{v,i}$ means for the volume concentration; $r_{V,i}$ means the median

221   radius, and σ_i means the standard deviation.

222   The volume median radius is computed by fine and coarse modes

223   particles as follows:

224
$$\ln r_V = \frac{\int_{r_{min}}^{r_{max}} \ln r \frac{dV(r)}{d\ln r} d\ln r}{\int_{r_{min}}^{r_{max}} \frac{dV(r)}{d\ln r} d\ln r} \tag{3}$$

225   Then the standard deviation is calculated from the volume median radius:

226
$$\sigma_V = \sqrt{\frac{\int_{r_{min}}^{r_{max}} (\ln r - \ln r_V)^2 \frac{dV(r)}{d\ln r} d\ln r}{\int_{r_{min}}^{r_{max}} \frac{dV(r)}{d\ln r} d\ln r}} \tag{4}$$

227   The volume concentration (μm^3/μm^2) is speculated by the following

228   equation:

229
$$C_V = \int_{r_{min}}^{r_{max}} \frac{dV(r)}{d\ln r} d\ln r \tag{5}$$

230   The SSA was retrieved only for $AOD_{440nm} > 0.40$; this was done to avoid

231   the larger uncertainty inherent in the lower AOD retrieval according to Dubovik

232   et al. (2002, 2006). The AAOD and AAE for wavelength λ were calculated as

233   follows:

234     $AAOD(\lambda) = [1 - SSA(\lambda)] \times AOD(\lambda)$ (6)

235    $$AAE = \frac{-\text{dln}[AAOD(\lambda)]}{\text{dln}(\lambda)} \qquad (7)$$

236   The total AODs' uncertainty was 0.01 to 0.02 according to Eck et al.

237   (1999). The accuracy of SSA retrieved from $AOD_{440nm} > 0.50$ with solar zenith

238   angles > 50 was 0.03 (Dubovik et al., 2002). The accuracy of the particle

239   volume size distribution was 15–25% between 0.1 μm $\leq$ r $\leq$ 7.0 μm and 25–100%

240   in conditions of r < 0.1 μm and r >7μm.

241   Direct aerosol radiative effect (DARE in W/m^2) was calculated by the

242   radiative transfer module under cloud-free conditions, which is similar to the

243   inversion of AERONET (García et al., 2008; 2012). The DARE at the bottom of

244   the atmosphere (BOA) and the top of the atmosphere (TOA) was defined as

245   the difference in the shortwave radiative fluxes with and without aerosol effects

246   as follows:

247

248    $$DARE_{TOA} = F_{TOA}^{\uparrow 0} - F_{TOA}^{\uparrow} \qquad (8)$$

249

250    $$DARE_{BOA} = F_{BOA}^{\downarrow} - F_{BOA}^{\downarrow 0} \qquad (9)$$

251

252   Where F and F^0 denoted the broadband fluxes including and excluding

253   aerosols, respectively at the BOA and TOA. The "↑" and "↓"mean the

254   downward fluxes and upward fluxes, respectively.

255   In the radiative transfer module, the absorption and multiple scattering

256   effects are taken into account during flux calculations by the Discrete

257   Ordinates (DISORT) approach (Nakajima and Tanaka, 1988; Stamnes et al.,

258   1988). The gaseous distributions and single fixed aerosol vertical distribution

259   (exponential to 1 km) from the multi-layered US standard 1976 atmosphere

260   were used in the radiative flux calculations (García et al., 2008). The error for

261   the observed solar radiation at the surface in global was +2.1 ± 3.0% for an

262   overestimation of about +9 ± 12 Wm^{-2}. The data used in preparing the figures

263   for the present paper have been made available as an Appendix.

264

3. Results and discussion

3.1 Spatial distribution of aerosol microphysical properties

267   A map showing the 50 CARSNET sampling sites and plots of the aerosol

268 volume size distributions (dV/dlnr) at each of the sites is shown in Fig. 1.

269 Generally, the annual mean effective radius of total particles (R_{effT}) decreased

270 from the inland northwest to the southeastern coastal areas. Furthermore, the

271 volume concentration of total particles was found to be substantially higher at

272 the urban sites. The volume of the coarse mode particles was considerably

273 larger than that of the fine mode particles at the remotes, arid/semi-arid sites

274 and at those sites on the CLP-Chinese Loess Plateau or nearby, indicating that

275 those areas were most strongly affected by larger particles, most likely mineral

276 dust as discussed below.

277   The average (arithmetic mean) R_{effT} at the remote sites was about 0.47

278 μm with the volume about 0.05 $μm^3/μm^2$ (Table 1). A large R_{effT} (0.64 μm) was

279 found at Lhasa, and the total aerosol volume there was 0.05 $μm^3/μm^2$. These

280 results are consistent with those reports by Li et al. (2018) who found high

281 levels of coarse mode particles at Lhasa due to the presence of mineral dust.

282 The two other remote sites, Akedala and Shangri-La, had smaller average R_{effT}

283 values than Lhasa (0.36 and 0.39 μm, respectively), and corresponding

284 volumes were 0.06 and 0.03 $μm^3/μm^2$. The average fine-mode effective radius

285 (R_{effF}) was 0.14 μm at the remote sites, and fine-mode particle fractional

286 volume (PV_F) was 0.01 $μm^3/μm^2$, while the average coarse-mode effective

287 radii (R_{effC}) was 2.35 μm and the coarse-mode fractional volume (PV_C) was

288 0.03 $μm^3/μm^2$. These findings indicated that the contribution of coarse-mode

289 particles to the total volume of aerosol was larger at the remote sites. A study

290 by Cong et al. (2009) at the remote Nam Co site on the Tibetan Plateau

291 showed that dust particles mainly affected the site in spring, while

292 anthropogenic aerosols were prevalent in the summer.

293   The average R_{effT} at the arid and semi-arid sites (0.55 μm) was larger than

294   at the remote sites, and the total volume of aerosols at the arid/semi-arid sites

295   also was large (0.14 $\mu m^3/\mu m^2$), nearly three times that at the remote sites.

296   Large R_{effT} values (0.71 μm) were found at Tazhong, which is near the

297   northwestern deserts, and the aerosol volume there also was high, 0.30

298    $\mu m^3/\mu m^2$. Large PV_C's were found at the arid/semi-arid sites (0.05–0.27

299    $\mu m^3/\mu m^2$). The arithmetic mean R_{effT} (0.49 μm) at the rural sites on or near the

300   CLP had total aerosol volumes (0.15 $\mu m^3/\mu m^2$) similar to those at the

301   arid/semi-arid sites. These results also show a major contribution to the

302   aerosol volumes by coarse-mode particles at the sites in or near the mineral

303   dust source regions. Bi et al. (2011) similarly found that coarse particles

304   dominated the volume-size distribution at the Semi-Arid Climate and

305   Environment Observatory of Lanzhou University (SACOL) on the CLP.

306   Small R_{effT} values (0.33 μm) were found at the rural sites in eastern China,

307   and relatively high aerosol volumes were observed there (0.18 $\mu m^3/\mu m^2$). In

308   the Yangtze River Delta (YRD) region, the R_{effF} was large range for 0.16–0.17

309   μm, and the PV_F's were 0.12–0.13 $\mu m^3/\mu m^2$. At the Mt. Longfeng background

310   site in northeastern China, the total particle volume was low (0.08 $\mu m^3/\mu m^2$),

311   which is consistent with minimal anthropogenic influences and low aerosol

312   loadings. Compared with the other sites, the urban areas had relatively low

313   coarse mode aerosol concentrations, but small particles were plentiful—the

314   average R_{effT} was 0.37 μm and total volume was high at 0.21 $\mu m^3/\mu m^2$. The

315   average R_{effF} of fine-mode particles at the urban sites was 0.16 μm with a PV_F

316   of 0.10 $\mu m^3/\mu m^2$ while the R_{effC} was 2.22 μm and PV_C was 0.11 $\mu m^3/\mu m^2$.

317   The effective radii and PV_F values showed strong relationships with

318   population density and vehicle emissions at the urban sites. High volumes of

319   fine mode particles occurred at the northeastern urban site of Shenyang (R_{effT}

320   = 0.16 μm, PV_F = 0.12 $\mu m^3/\mu m^2$); at major cities in northern China, including

321   Shijiazhuang (R_{effT} = 0.16 μm, PV_F = 0.12 $\mu m^3/\mu m^2$) and Zhengzhou (R_{effT} =

322   0.18 μm, PV_F = 0.12 $\mu m^3/\mu m^2$); at Chengdu, a city in the Sichuan Basin of

323   (R_{effT} = 0.21 μm, PV_F = 0.16 $\mu m^3/\mu m^2$); and at the urban regions of Nanning

324 (R_{effT} = 0.18 µm, PV_F = 0.13 µm³/µm²) and Panyu (R_{effT} = 0.16 µm, PV_F = 0.10

325 µm³/µm²) in southern China. Overall, these results show that the volumes of

326 fine-mode particles increased at the urban sites where anthropogenic

327 influences were most apparent.

328   Cheng et al. (2015) found different aerosol volume size distributions for

329 dust and sea salt at Shanghai in the eastern China, and they showed that their

330 relative abundances varied with season and in response to local or long-range

331 transport. Zhao et al. (2018) also reported the influence of sea salt aerosol on

332 the coast of northeastern China. Che et al. (2018) found that aerosol

333 hygroscopicity affected the aerosol microphysical properties in the YRD region.

334 These findings suggest that the hygroscopic growth of fine-mode particles can

335 affect aerosol microphysical properties and that differences in climatic

336 conditions could lead to geographically variable effects.

337

338 **3.2 Spatial distributions of AOD and EAE**

339   The spatial distributions of $AOD_{440\,nm}$ and $EAE_{440-870\,nm}$ are shown in Fig. 2.

340 The AOD_{440nm} increased from the remote/rural sites to the urban sites, and as

341 one might expect, the remote sites were the least affected by particle

342 emissions and had the lowest aerosol loadings. For example, the AOD_{440nm} at

343 the remote stations was low and had an average value of 0.12. The Lhasa and

344 Shangri-La sites on the Tibetan Plateau had similar average AOD_{440nm} values

345 of 0.10. These phenomenons are similar to the study of Li et al. (2018), who

346 showed clean air conditions at Lhasa with AOD < 0.1. Cong et al. (2007, 2009)

347 also found a low AOD (0.05) at Nam Co, which was comparable to the

348 background levels at other remote sites.

349   The AOD_{440nm}'s at the arid/semi-arid sites and those on or near the Loess

350 Plateau ranged from 0.32–0.42, which is higher than at the remote sites. The

351 high AOD_{440nm} at Tazhong (0.60), which is near the deserts in northwestern

352 China was likely due to the large aerosol volume of 0.30 µm³/µm² (section 3.1)

353 caused by mineral dust. Indeed, arid and semi-arid regions in northwestern

354 China are important sources of aeolian dust on a global scale (Bi et al., 2011).

355 Li et al. (2012) showed that the contribution of dust to the average AOD at

356 SACOL near Lanzhou was 28.4%. Other sites that showed large AOD_{440nm}

357 include regions with strong anthropogenic influences, such as Dengfeng (0.79)

358 on the North China Plain, Huimin (0.83) in the YRD (0.83 to 0.87) and Huainan

359 (0.91) in the Guanzhong Plain.

360   Compared with the sites just discussed, lower AOD_{440nm}'s were found at

361 the Mt. Longfeng background station of the Northeast China Plain (0.34), the

362 semi-arid rural site as Tongyu in northeastern China (0.23), and the clean

363 Xiyong site in southern China (0.41). Zhu et al. (2014) found a low AOD of 0.28

364 at the North China Plain regional background site. Che et al. (2009c) have

365 pointed out that the large AOD at Lin'an was likely affected by the high aerosol

366 loadings in YRD Region. Among the urban sites in China, large $AOD4_{40nm}$'s

367 were found in the cities with strong influences of anthropogenic activities, such

368 as the Northeastern Plain (Shenyang 0.89), North China Plain (Zhengzhou

369 0.99), YRD region (Wuhan 1.00) and Sichuan Basin (Chengdu 1.17); the

370 average value for these sites was 0.79. Lower AOD_{440nm}'s, that is < 0.50,

371 occurred at remote sites in northwestern China, including Urumqi (0.42),

372 Yinchuan (0.37); those sites are affected less by industrial activities and the

373 population densities are lower compared with the sites in northern or eastern

374 China.

375   It is worth noting that the particle emissions in and around the urban sites

376 could lead to large optical extinctions due to hygroscopic aerosol growth,

377 especially in summer when the relative humidity is often high. In a related

378 study, Zhang et al. (2018) found a large AOD of 1.10 at Wuhan in central China

379 and that was linked to secondary aerosol formation under the high

380 summertime temperatures. Li et al. (2015) similarly concluded that high

381 temperature and humidity promoted the formation of fine particles and led to

382 hygroscopic aerosol growth at Nanjing. Qin et al. (2017) observed a high

383 $AOD_{500\ nm}$ of 1.04 at Shijiazhuang and related this to the hygroscopic growth of

384   aerosol fine-mode particles during polluted days.

385   Clear spatial variability in EAE values over China is evident in Fig. 3, and

386   at the remote sites, the average EAEs were 1.03. The EAE at Lhasa (0.77)

387   was lower than at Akedala (EAE = 1.13), which is in an arid region of central

388   Asia, or at Shangri-La (EAE = 1.19) in Tibet. The average coarse-mode

389   average effective radii (R_{effC}) at Lhasa was 2.26 μm and the fractional volume

390   was 0.04 μm^3/μm^2, this result suggests the major components of the large

391   mineral dust particles in aerosol populations over that region. The smaller

392   sphericity fraction (~42.70) and lower FMF (0.66) at Lhasa indications the

393   presence of non-spherical aerosol coarse particles compared with the

394   spherical fine particles in the urban sites.

395   At the arid and semi-arid sites in China, the average EAE value (0.71) was

396   relatively low and the FMF also was low (0.58). The EAE was extremely low at

397   Tazhong (0.25), which is in the Takliman Desert in the Xinjiang Uygur

398   Autonomous Region of northwestern China and the sphericity fraction (12.87)

399   and FMF (0.35) there were lower compared with most of the other sites. This

400   finding indicates a strong contribution of large particles in this desert region

401   consistent with large volume of the coarse-mode particles (0.27 μm^3/μm^2)

402   noted in section 3.1. The average EAE reached 0.93 at the rural sites near the

403   CLP, and the average value of FMF for those sites was 0.73. Eck et al. (2005)

404   found especially low EAE values in March and April (0.3 and 0.4, respectively)

405   at Yulin, China, where the dust aerosol dominated the optical column.

406   Large EAEs (1.23) were found at the sites in eastern China, and the FMFs

407   also were large (0.89) at those sites. This result can be attributed to the strong

408   impacts of anthropogenic in the more urbanized eastern part of the country. On

409   the other hand, large EAE values also occurred at the clean sites in

410   northeastern China, including Mt. Longfeng (1.38), where the sphericity

411   fraction was 58.5 and the FMF 0.90. This shows that small particles can have

412   stronger effects in these areas relative to some other regions of China. The

413   EAE at Lin'an was larger than that at Shangdianzi in the Northern Plain or

Longfengshan in Northeastern China for most months according to data from
Che et al. (2009c). At the urban sites, large EAEs were found at sites in
southern China, including Nanning (EAE = 1.36, sphericity fraction = 70.12,
FMF = 0.95), Panyu (EAE = 1.43, sphericity fraction = 75.55, FMF = 0.93) and
Zhuzilin (EAE = 1.45, sphericity fraction = 55.51, FMF = 0.94). This is likely
because the large populations and widespread vehicle ownership in those
cities led to the dominance of fine-mode particles throughout the year. Cheng
et al. (2015) found a uni-modal distribution of EAE centered in 1.1–1.6 with the
occurrence frequency about 72%, which indicated an abundance of fine
primary particles at Shanghai in eastern China. At the urban Nanjing site,
which is in east-central China, small particles were dominant, and the annual
average EAE was 1.21 ± 0.28 (Li et al., 2015).

3.3 Spatial distribution of aerosol single-scattering albedo

The spatial distribution of SSA at 440 nm of the 50 CARSNET stations is
shown in Fig. 4. As a frame of reference, Eck et al. (2005) reported that that
SSA_{440nm} from the AERONET retrievals were 0.82 to 0.98 globally. We note
that SSA_{440nm} values in this range reflect slightly to strongly absorbing aerosols,
and these particles originate from a multitude of sources (Che et al., 2018).
The SSA_{440nm}'s decreased from remote/rural to the urban sites and from west
to east, which means that there were higher percentages of absorbing
particles at the urban and eastern stations. The average SSA_{440nm} at the
remote sites was about 0.91, which is indicative of particles with moderate
absorption. The absorbing aerosols at the remote sites were more than likely
mineral dust particles because those sites are less likely to be affected by
carbonaceous particles, which also are absorbing, but mainly produced by
anthropogenic activities. The SSA_{440nm}'s for the arid and semi-arid sites were
0.89. The relatively high SSA at Tazhong (0.92) was probably due to slightly
absorbing, coarse mode dust particles (EAE 0.25).

A study by Bi et al. (2011) showed that SSAs increased slightly with

444 wavelength when dust was present at the SACOL site. Moderately absorbing

445 particles were found in our study on or near the Chinese Loess Plateau where

446 the SSA_{440nm}'s were typically 0.88 to 0.89. Eck et al. (2005) concluded that the

447 spectral SSA demonstrated effects of dust at Yulin because the SSA increased

448 for wavelengths from 440 to 675 nm. At the rural sites in eastern China, large

449 SSA_{440nm}'s mainly occurred at sites in the YRD affected anthropogenic

450 influences; these include Tonglu (0.93), Xiaoshan (0.93), Xiyong (0.94). Che et

451 al. (2018) found the slightly absorbing particles came from industrial activity

452 and anthropogenic sources at YRD region with the $SSA_{440\,nm}$ between 0.91 to

453 0.94.

454   The average value of SSA_{440nm} at the urban sites was 0.90, which

455 indicates that particles with moderate absorption dominated the aerosol

456 populations. Cheng et al. (2015) reported a seasonal range of SSA from 0.88

457 to 0.91 at Shanghai, with higher values in autumn and winter compared with

458 spring and summer. Lower SSA_{440nm}'s occurred at the urban sites and

459 industrial regions in northeastern China, such as Shenyang (0.84), Anshan

460 (0.89), Fuhsun (0.84), which indicates that the particles were more strongly

461 absorbing in that region. On the other hand, higher SSA_{440n}'s were found at

462 urban sites in southern China, including Nanning (0.92), Panyu (0.90) and

463 Zhuzilin (0.96), and this indicates that the particles at those sites were slightly

464 or weakly absorbing.

465   Moreover, we found that the SSA_{440nm} spatial distribution reflected the

466 percentages of absorbing aerosols at the urban sites both in northern and

467 eastern China. The reports of Dubovik et al. (2000, 2002, 2006) showed that

468 SSA values vary with both particle size and composition, and Su et al. (2017)

469 used the variations in SSA with wavelength to indicate the presence of brown

470 carbon aerosols at Tianjin, a coastal megacity in China. Qin et al. (2017)

471 suggested that the small SSAs found at Shijiazhuang indicated the presence

472 of fine-mode absorbing particles, such as brown carbon. Zhuang et al. (2014)

473 reported that the SSA at the Nanjing urban site ranged from 0.90 to 0.95, and

474   the aerosol was more absorbing in fall, possibly due to the biomass burning

475   emission in the YRD. As evident in the results presented in section 3.1, one

476   can see that the R_{effT}, R_{effF} and R_{effC} between northeastern and southern China

477   was very similar. For example, at Shenyang, a megacity in northeastern China,

478   the effective radii of total, fine- and coarse-mode particles were 0.31, 0.16,

479   2.23 μm and the corresponding volumes were 0.22, 0.12, 0.10 $μm^3/μm^2$,

480   respectively. At Hangzhou in the YRD region, the R_{effT}, R_{effF} and R_{effC} were 0.30,

481   0.17, 2.21 μm with the volumes about 0.22, 0.12, 0.10 $μm^3/μm^2$, respectively.

482   Therefore, the different SSA_{440nm} distributions in the two regions may be

483   attributed by the special aerosol composition.

484   Dust aerosols with light-absorbing occur more frequently in spring in

485   northeastern China than in more southern regions (Zhao et al., 2018).

486   Anthropogenic emissions from seasonal biomass burning and residential

487   heating are two other main factors that affect aerosol composition between the

488   two regions (Che et al., 2018). Especially in winter, there was high percentage

489   of absorbing aerosols at the northeastern sites, and that was more than likely

490   caused by emissions of carbonaceous aerosol from residential heating (Zhao

491   et al., 2015). Climatic conditions are also the main factors affecting the

492   absorption characteristics of aerosols in different regions of north and south

493   China. The increased light scattering could well be due to the particles

494   hygroscopic growth demonstrated in other studies. For example, Mai et al.

495   (2018) found that AODs and SSAs both increased with relative humidity at

496   Guangdong in the PRD region, which suggests that condensational growth

497   can affect the aerosol optical properties.

498

499   **3.4 Spatial distributions of absorption aerosol optical depth (AAOD)**

500   The spatial distribution of AAOD at 440 nm shown as Fig. 5 indicates that

501   overall, the $AAOD_{440nm}$'s increased from north to south and from remote/rural

502   to urban sites. Lower $AAOD_{440nm}$'s were found at the remote stations, where

503   the average value was 0.01. The $AAOD_{440nm}$ at Akedala, a remote site in

northwestern China, was 0.02, and that was higher than at Shangri-La or Lhasa (0.01), both of which are on the Tibetan Plateau. The low $AAOD_{440nm}$'s throughout that region indicates that the aerosol population was not strongly absorbing. Compared with these three sites, the average $AAOD_{440nm}$'s at the arid and semi-arid sites were higher (0.03); for example, an $AAOD_{440nm}$ of 0.05was found at Tazhong, which is adjacent to the desert, and that indicates that the aerosol particles were more absorbing. As discussed in sections 3.2 and 3.3, dust aerosols likely make a significant contribution to aerosol light absorption in the areas impacted by the deserts.

The low $AAOD_{440nm}$ found at Xilinhot (0.02) was probably due to the low aerosol loadings (AOD_{440nm} = 0.21) in this region. The $AAOD_{440nm}$'s at the Mt. Gaolan and Yulin rural sites which on or around the CLP were about 0.04 and 0.03, respectively, and the particles were moderately absorbing (SSA = 0.89). The large $AAOD_{440nm}$ at Datong (0.09) can be explained by the high AOD_{440nm} (0.58) there. Indeed, large $AAOD_{440nm}$'s were found at rural sites in eastern China, where there were high AODs and low SSAs as noted in sections 3.2 and 3.3. Of these sites, Dengfeng (AOD_{440nm} = 0.08) and Huimin (AOD_{440nm} = 0.08) are located on the North China Plain, while Huainan (AOD_{440nm} = 0.10) is on the Guanzhong Plain. Lower $AAOD_{440nm}$'s, from 0.02–0.03, occurred at Tongyu (0.03), which is at a semi-arid region in northeastern China, at the Mt. Longfeng (0.03) regional background site on the Northeast China Plain, at the Yushe rural site in northern China (0.03), and at the clean Xiyong site in the PRD (0.02).

Several urban sites showed $AAOD_{440nm}$ values greater than 0.10; these include Fushun (0.11) and Shenyang (0.14) in the northeastern China, Lanzhou (0.10) in the northwestern China, and Nanjing (0.10) and Wuhan (0.11) in the eastern China. Lower $AAOD_{440nm}$'s occurred in other urban areas, such as Yinchuan ($AAOD_{440nm}$ = 0.02, AOD_{440nm} = 0.37) in the northwest and Zhuzilin ($AAOD_{440nm}$ = 0.03, AOD_{440nm} = 0.66) in the PRD; both of these sites had relatively low AOD_{440}'s indicating weaker anthropogenic influences

534 compared with metropolitan regions of some other areas. We note that there

535 are significant uncertainties in relating aerosol absorbing properties to particle

536 types, such as black carbon, organic matter, as well as mineral dust (Russell et

537 al., 2010; Giles et al., 2012). Nonetheless, the information presented here on

538 the spatial distribution of AAODs over China may be useful for the further

539 investigations into the relationships between light absorption and particle type

540 (Liu et al., 2017; Schuster et al., 2016a, 2016b).

541

542 3.5 Spatial distribution of aerosol direct radiative effect at the Earth's

543 surface and top of the atmosphere

544   The spatial distributions of the DAREs calculated for both the bottom and

545 top of the atmosphere are shown in Fig. 6. Overall, the DARE-BOAs increased

546 from northwest to southeast and from rural to urban sites, consistent with

547 impacts from the densely populated regions around the sites. The average

548 DARE-BOA at the remote sites was -24.40 W/m^2, and in comparison, a higher

549 DARE-BOA (-33.65 W/m^2) occurred at Akedala, which occurred on a remote

550 region of northwestern China. The AOD_{440nm} at Akedala was relatively low

551 (0.17) and the SSA moderate (0.90). The moderate absorption of aerosol could

552 lead to more strong surface cooling effects with little higher DARE-BOA than

553 the other remote sites. The DARE-BOAs for Lhasa and Shangri-La were

554 -22.13 and -17.43, respectively. These results indicate weaker surface cooling

555 effects at the remote sites relative to other regions because the aerosol

556 loadings were relatively low, as indicated by AOD_{440nm}'s < 0.20.

557   The average DARE-BOTs at the arid and semi-arid sites of China were

558 about -56.43 W/m^2, and those high DARE-BOAs can be explained by the

559 moderately absorbing particles (SSA = 0.89) and large AOD_{440nm}'s (0.32)

560 compared with the remote sites. A large DARE-BOA (-91.20 W/m^2) occurred at

561 the Tazhong site near the northwestern deserts, and there, the high AOD (0.60)

562 and the slight absorption of mineral dust (SSA = 0.92) imply substantial surface

563 cooling. The average DARE-BOA for rural sites on the Chinese Loess Plateau

564   or surrounding was -74.67 W/m^2, and that also implies cooling at the surface.

565   Several rural sites in northern and eastern China had large DARE-BOA

566   values; these include Huimin (-111.58 W/m^2), Dengfeng (-104.78 W/m^2) and

567   Huainan (-129.17 W/m^2), and at those sites the AODs were high, from 0.80–

568   0.90, and the SSAs were ~0.89. These results show stronger surface cooling

569   effects at sites influenced by anthropogenic emissions compared with the

570   remote sites or those near the deserts. The large negative DARE-BOA values

571   (-103.28 W/m^2) at the urban sites indicate that the combination of high

572   AOD$_{440nm}$'s (0.79) and moderate SSAs (0.90) can cause significant surface

573   cooling. Indeed, anthropogenic emissions presumably led to the high

574   DARE-BOAs at urban sites, including Shenyang (-144.88 W/m^2) and Fushun

575   (-116.91 W/m^2) in the Northeastern Plain, Xian in the Guanzhong Plain

576   (-132.55 W/m^2), Chengdu in the Sichuan Basin (-110.42 W/m^2), Lanzhou in the

577   western region (-126.17 W/m^2), and Nanjing (-143.38 W/m^2) and Wuhan

578   (-171.80 W/m^2) in the YRD. These results indicate that anthropogenic aerosols

579   can cause significant direct radiative effects at urban sites.

580   The DARE-TOAs increased from north to south and from rural to urban

581   sites, and the average DARE-TOA for the remote stations was low, about -4.79

582   W/m^2 (Fig. 7). The DARE-TOAs at Lhasa and Shangri-La were -5.04 W/m^2

583   and -8.93 W/m^2, respectively. A notably small DARE-TOA was found at

584   Akedala (0.42 W/m^2), indicating that the effects of the aerosol on the

585   temperature of earth-atmosphere system there would be weak. The average

586   DARE-TOA at the arid and semi-arid sites was -10.17 W/m^2. The large

587   DARE-TOA found at Tazhong (-23.49 W/m^2) could represent the larger

588   contribution of slightly absorbing mineral aerosols (SSA 0.92) and a large AOD

589   (0.60); this indicates more cooling at surface through the absorption and

590   scattering solar radiation compared with the less impacted sites. This is

591   consistent with the results for Tazhong discussed in section 3.1 which showed

592   high volumes of coarse mode particles with large radii.

593   The average DARE-TOA at rural sites on the Chinese Loess Plateau or

594   nearby was about -14.56 W/m^2. Although the SSA$_{440nm}$ were close to Gaolan

595   and Yulin about 0.89, the TOAs were quite different (Mt. Gaolan -20.87 W/m^2;

596   Yulin -9.09 W/m^2) which could be due to the different AOD$_{440nm}$ about 0.36 and

597   0.32, respectively. In rural eastern China, the DARE-TOA was about -32.40

598   W/m^2, and to put this in context, Che et al. (2018) found that DARE-TOAs of

599   −40 W/m^2 at rural sites in the YRD region, which is indicative of a relatively

600   strong cooling effect. Low DARE-TOAs were found at the Mt. Longfeng rural

601   site in northeastern China (DARE-TOA = -11.34, AOD$_{440nm}$ = 0.34, SSA = 0.89)

602   and at the Tongyu semi-arid site in northeastern China as (DARE-TOA = -8.87,

603   AOD$_{440nm}$ = 0.23, SSA = 0.88) where the aerosol loadings were relatively low

604   and the absorption was moderate.

605   In the urban sites at central and eastern China, the average DARE-TOA

606   values were about -30.05 W/m^2. Higher DARE-TOAs occurred at Anshan in

607   the Northeastern Plain (-39.66 W/m^2), Chengdu in the Sichuan Basin as

608   (-52.21 W/m^2), Hangzhou in the YRD (-40.16 W/m^2), Jiaozuo (-39.35 W/m^2)

609   and Zhengzhou (-46.18 W/m^2) in the North China Plain, and Zhuzilin (-40.15

610   W/m^2) in the PRD region. The high DARE-TOA values at these urban sites

611   imply relatively strong cooling effects due to moderate to strong light

612   absorption by the particles.

613

614   **3.6 Spatial distributions of aerosol mixing properties**

615   The spatial distribution of aerosol mixing properties (Figure 8) was

616   obtained by using the SSA$_{440nm}$, FMF, and EAE results to classify the particles

617   based on size and absorbing properties. In previous studies by Zheng et al.

618   (2017) and Che et al. (2018), the particles in this study were grouped into eight

619   types as Table 2 show. Moreover, the FMF has been provided to give the

620   particle size information in the group of the particles.

621   At the remote Akedala and Lhasa sites (FMF = 0.70–0.78 and SSA$_{440nm}$ =

622   0.85), the percentages of mixed absorbing particles (Type V) were 35-40%,

623   while at Shangri-la (FMF = 0.76, SSA$_{440nm}$ = 0.84), the percentage was slightly

624 lower, 24.62%. The characteristics of the particles at these remote,
625 high-altitude sites were probably affected by the rugged topography which
626 would promote particle mixing. The proportion of coarse mode, mainly dust,
627 particles with moderate to strong absorption (Group VII) was highest at the arid
628 and semi-arid sites. The percent abundances of Group VII particles were 57.90%
629 at Dunhuang (AE = 0.26, SSA_{440nm} = 0.85, FMF = 0.43) and 58.52% at
630 Tazhong (AE = 0.20, SSA_{440nm} = 0.87, FMF = 0.37), respectively. Mixed
631 absorbing particles (Type V) and strongly absorbing dust particles (Group VII)
632 accounted for 30 to 70% of the aerosol in the rural sites on or near the CLP.
633 The percentages of mixed absorbing particles (Type V) at Gaolan, Yulin, and
634 Datong were 31.98%, 45.22% and 29.04%, respectively, and the average
635 FMFs at those sites ranged from 0.70–0.76.

636   The proportions of the coarse-mode aerosols with strongly absorbing in
637 Group VII were about 35.23% at Gaolan and 21.21% at Yulin, which was
638 mainly dust particles with the FMFs at those sites were 0.43 and 0.48,
639 respectively. The proportion of coarse-mode particles with strongly absorbing
640 in Group VII and coarse-mode particles with weakly-absorbing in Group VIII at
641 the rural sites in eastern China were < 11%. These patterns indicated that the
642 differences in the eastern region from northwestern China because in the east,
643 coarse-mode particles have only a minor contribution to aerosol absorption.
644 The percentage of fine-mode particles with weakly-absorbing in Type IV and
645 mixed absorbing particles in Type V combined about ~50% at the eastern sites.
646 This result suggests that mixed aerosols originated from a variety of sources
647 and that many of the sites were affected by anthropogenic emissions from
648 megacities upwind.

649   The fine-mode particles with absorbing in Types I, II, III and V accounted
650 for 50 to 90% at most of the urban sites. The percentages of these four particle
651 types combined were especially large in eastern China; for example, at Panyu,
652 particle Types I—IV composed 90.83% of the total, and the FMF there was
653 0.90–0.94, while at Zhuzilin, the percentage of Types I–IV was 92.55%, and

654   the FMF was 0.92–0.94. These results are another indication that fine-mode

655   particles are important for light absorption in urban areas. In contrast, the

656   Lanzhou and Urumqi urban sites were less affected by absorbing fine-particles

657   because the percentages of Type I–IV particles were only 19.73% and 18.36%,

658   respectively. The mixed absorbing Type V particles accounted for large

659   percentages of the total at Lanzhou (48.80%, EAE = 0.88, SSA = 0.82, FMF =

660   0.73) and at Urumqi (59.39%, EAE = 0.94, SSA = 0.84, FMF = 0.75). Different

661   from the other urban sites, these patterns show that larger particles had

662   significant contributions to the aerosol absorption at these two northwestern

663   sites.

664

4. Conclusions

665

666   Aerosol microphysical and its optical properties obtained from the

667   ground-based sunphotometer deployed at 50 CARSNET stations were used to

668   begin the development of their climatology characteristics and to investigate

669   potential aerosol-climate effects over vast area of China. Direct aerosol

670   radiative effects (DAREs) at the bottom and at the top of the atmosphere were

671   calculated, and eight types of aerosols were classified based on the particle

672   size and absorbing properties. The annual mean values of the ReffT

673   decreased from the arid and semi-arid sites (0.55 μm) to the urban sites (0.37

674   μm). The aerosol volumes increased from the remote sites (0.05 $\mu m^3/\mu m^2$) to

675   the urban sites (0.21 $\mu m^3/\mu m^2$). The volumes of coarse-mode particle were

676   larger than those for the fine mode at the remote and arid/semi-arid sites—this

677   can be explained by the greater relative abundances of mineral dust compared

678   with pollution-derived particles at those sites. At the urban sites, where

679   anthropogenic influences were relatively strong, the proportion of fine mode

680   particles increased gradually with aerosol volume.

681   The AOD_{440nm} progressively increased from the remote sites (0.12) to the

682   arid and semi-arid sites (0.32) to rural sites in eastern China (0.70) and finally

683   to the urban sites (0.79), which were the ones most strongly affected by

684 anthropogenic activities. The average $EAE_{440\text{-}870\ nm}$'s at the arid and semi-arid

685 sites were relatively low (0.71), which indicates an important contribution of

686 larger particles to the aerosol extinction in those regions. The consistently

687 large $EAE_{440\text{-}870\ nm}$'s at the urban sites (> 1.20) and the high FMFs that those

688 site (0.88) are the evidence that fine mode particles are prevalent throughout

689 year. The average SSA_{440nm}'s at the remote, rural, and urban sites were

690 relatively similar, averaging about 0.89, and this indicates the particles were

691 moderately absorbing.

692 Overall, dust aerosols with light-absorbing in spring and emissions came

693 from biomass burning and residential heating during the colder months were

694 the main factors that led to spatial differences in the percentages of absorbing

695 aerosols over China. The $AAOD_{440nm}$'s increased from the remote sites (0.01)

696 to the arid and semi-arid sites (0.03) to the rural sites of eastern China (0.05)

697 and finally to the urban sites (0.07). High $AAOD_{440nm}$'s were caused by

698 light-absorbing dust aerosols at the rural sites and by the strong anthropogenic

699 emissions in the metropolitan areas. The spatial patterns in the absorbing

700 aerosols were not only affected by the chemical composition of aerosol, but

701 also by physical effects imposed by topography, weather, and climate.

702 The average DARE-BOA values were -24.40 W/m^2 at the remote sites;

703 -56.43 W/m^2 at the arid and semi-arid sites; -74.67 W/m^2 at the sites on the

704 CLP or nearby; -85.25 W/m^2 at the rural sites in eastern China; and -103.28

705 W/m^2 at the urban sites. The larger DARE-BOA values at the urban sites imply

706 stronger cooling effects from anthropogenic emissions compared with those

707 from mineral dust at the remote sites or those near the desert. Moreover, larger

708 DARE-TOA's also occurred at the urban sites (-30.05 W/m^2), which indicates

709 strong cooling effects due to the large aerosol extinctions between the

710 earth-atmosphere system displayed the moderate to strong light absorption.

711 Mixed-absorbing particles were the most abundant aerosol type in the remote

712 and rural sites on or near the Chinese Loess Plateau and in eastern China.

713 Mineral dust particles with moderate to strong absorbing were dominant in the

714 arid and semi-arid sites while absorbing fine-mode particles accounted for 50

715 to 90% of the aerosol at the most urban sites.

716   The results of the study have considerable value for ground truthing

717 satellite observations and for validating aerosol models. Moreover, the results

718 also have provided significant information on aerosol optical and radiative

719 properties for different types of sites covering a broad expanse of China.

720 These results also are a major step towards developing a climatology for

721 aerosol microphysical and optical properties for China and even East Asia.

722 **Data availability:**

723   The detailed CARSNET AOD dataset used in the study can be requested

724 by contacting the corresponding author.

725 **Competing interests.**

726   The authors declare that they have no conflict of interest.

727 **Author contribution:**

728   All authors contributed to shaping up the ideas and reviewing the paper.

729 HC, XX and XZ designed and implemented the research, as well as prepared

730 the manuscript; HC, HZ,YW and HW contributed to analysis of the CARSNET

731 dataset; HC, XX, JZ, OD, BNH, PG, and ECA contributed to the CARSNET

732 data retrieval; HC, BQ, WG, HY, RZ, LY, JC, YZ, KG, and XZ carried out the

733 CARSNET observations; OD, BNH, PG, and ECA provided constructive

734 comments on this research.

735 **Acknowledgments**

736   This work was supported by grants from the National Science Fund for

737 Distinguished Young Scholars (41825011), the National Key R & D Program

738 Pilot Projects of China (2016YFA0601901), National Natural Science

739 Foundation of China (41590874), the CAMS Basis Research Project

740 (2017Z011), the European Union Seventh Framework Programme

741 (FP7/2007-2013) under grant agreement no. 262254. AERONET-Europe

742 ACTRIS-2 program, European Union's Horizon 2020 research and innovation

743 programme under grant agreement No 654109.

744

745 **References**

746 Bi, J.R., Huang, J.P., Fu, Q., Wang, X., Shi, J.S., Zhang, W., Huang, Z.W., and

747 Zhang, B.D.: Toward characterization of the aerosol optical properties

748 over Loess Plateau of Northwestern China, Journal of Quantitative

749 Spectroscopy and Radiative Transfer, 112, 346-360,

750 https://doi.org/10.1016/j.jqsrt.2010.09.006, 2011.

751 Bokoye, A.I., Royer, A., O'Neill, N.T., Cliche, P., Fedosejevs, G., Teillet, P.M.,

752 and Mcarthur, L.J.B.: Characterization of atmospheric aerosols across

753 Canada from a Ground-based sun photometer network: Aerocan, Atmos.

754 Ocean., 39, 429–456, https://doi.org/10.1080/07055900.2001.9649687,

755 2001.

756 Breon, F., Tanré, D., and Generoso, S.: Aerosols effect on the cloud droplet

757 size monitored from satellite, Science, 295, 834-838,

758 https://doi.org/10.1126/science.1066434, 2002.

759 Cao, J.J., Lee, S.C., Chow, J.C., Watson, J.G., Ho, K.F., Zhang, R.J., Jin, Z.D.,

760 Shen, Z.X., Chen, G.C., Kang, Y.M., Zou, S.C., Zhang, L.Z., Qi, S.H., Dai,

761 M.H, Cheng, Y., and Hu, K.: Spatial and seasonal distributions of

762 carbonaceous aerosols over China, J. Geophys. Res., 112, D22S11.

763 http://dx.doi.org/10.1029/2006JD008205, 2007.

764 Charlson, R. J., Schwartz, S. E., Hales, J. M., Cess, D., Coakley, J. A., and

765 Hansen, J. E.: Climate forcing by anthropogenic aerosols, Science, 255,

766 423–430, https://doi.org/10.1126/science.255.5043.423, 1992.

767 Che, H.Z., Shi, G.Y., Zhang, X.Y., Arimoto, R., Zhao, J.Q., Xu, L., Wang, B.,

768 and Chen, Z.H.: Analysis of 40 years of solar radiation data from China,

769 1961-2000, Geophysical Research Letters, 32, L06803,

770 https://doi.org/10.1029/2004GL022322, 2005.

771 Che, H., Shi, G., Uchiyama, A., Yamazaki, A., Chen, H., Goloub, P., and Zhang,

772 X.: Intercomparison between aerosol optical properties by a PREDE

773 skyradiometer and CIMEL sunphotometer over Beijing, China, Atmos.

774   Chem. Phys., 8, 3199–3214, http://dx.doi.org/10.5194/acp-8-3199-2008,
775   2008.

776 Che, H., Zhang, X., Chen, H., Damiri, B., Goloub, P., Li, Z., Zhang, X., Wei, Y.,
777   Zhou, H., Dong, F., Li, D., and Zhou, T.: Instrument calibration and aerosol
778   optical depth (AOD) validation of the China Aerosol Remote Sensing
779   Network (CARSNET), J. Geophys. Res., 114, D03206,
780   https://doi.org/10.1029/2008JD011030, 2009a.

781 Che, H. Z., Zhang, X. Y., Alfraro, S., Chatenet, B., Gomes, L., and Zhao, J. Q.:
782   Aerosol optical properties and its radiative forcing over Yulin, China in
783   2001 and 2002, Adv. Atmos. Sci., 26, 564–576,
784   https://doi.org/10.1007/s00376-009-0564-4, 2009b.

785 Che, H. Z., Yang, Z. F., Zhang, X. Y., Zhu, C. Z., Ma, Q. L., Zhou, H. G., and
786   Wang, P.: Study on the aerosol optical properties and their relationship
787   with aerosol chemical compositions over three regional background
788   stations in China, Atmospheric Environment, 43, 1093–1099,
789   https://doi.org/10.1016/j.atmosenv.2008.11.010, 2009c.

790 Che, H., Xia, X., Zhu, J., Li, Z., Dubovik, O., Holben, B., Goloub, P., Chen, H.,
791   Estelles, V., Cuevas-Agulló, E., Blarel, L., Wang, H., Zhao, H., Zhang, X.,
792   Wang, Y., Sun, J., Tao, R., Zhang, X., and Shi, G.: Column aerosol optical
793   properties and aerosol radiative forcing during a serious haze-fog month
794   over North China Plain in 2013 based on ground-based sunphotometer
795   measurements, Atmos. Chem. Phys., 14, 2125–2138,
796   https://doi.org/10.5194/acp-14-2125-2014.

797 Che, H., Zhang, X.-Y., Xia, X., Goloub, P., Holben, B., Zhao, H., Wang, Y.,
798   Zhang, X.-C., Wang, H., Blarel, L., Damiri, B., Zhang, R., Deng, X., Ma, Y.,
799   Wang, T., Geng, F., Qi, B., Zhu, J., Yu, J., Chen, Q., and Shi, G.:
800   Ground-based aerosol climatology of China: aerosol optical depths from
801   the China Aerosol Remote Sensing Network (CARSNET) 2002–2013,
802   Atmos. Chem. Phys., 15, 7619–7652, https://doi.org/10.5194/acp-
803   15-7619-2015, 2015.

804 Che, H., Qi, B., Zhao, H., Xia, X., Eck, T.F., Goloub, P., Dubovik, O., Estelles,
805   V., Cuevas-Agulló, E., Blarel, L., Wu, Y., Zhu, J., Du, R., Wang, Y., Wang,
806   H., Gui, K., Yu, J., Zheng, Y., Sun, T., Chen, Q., Shi, G., and Zhang X.:
807   Aerosol optical properties and direct radiative forcing based on
808   measurements from the China Aerosol Remote Sensing Network
809   (CARSNET) in eastern China, Atmospheric Chemistry and Physics, 18,
810   405–425, https://doi.org/10.5194/acp-18-405-2018, 2018.

811 Cong, Z.Y., Kang, S.C., Liu, X.D., and Wang, G.F.: Elemental composition of
812   aerosol in the Nam Co region, Tibetan Plateau, during summer monsoon
813   season,   Atmospheric   Environment,   41,   1180–1187,
814   https://doi.org/10.1016/j.atmosenv.2006.09.046, 2007.

815 Cong, Z.Y., Kang, S.C., Smirnov, A., and Holben, B.: Aerosol optical properties
816   at Nam Co, a remote site in central Tibetan Plateau, Atmospheric
817   Research, 92, 42–48, https://doi.org/10.1016/j.atmosres.2008.08.005,
818   2009.

819 Duan, J. and Mao, J.: Study on the distribution and variation trends of
820   atmospheric aerosol optical depth over the Yangtze River Delta, Acta
821   Scien.   Circum.,   27,   537–543,
822   https://doi.org/10.1007/978-1-4020-6475-3_126, 2007.

823 Dubovik, O. and King, M. D.: A flexible inversion algorithm for retrieval of
824   aerosol optical properties from sun and sky radiance measurements, J.
825   Geophys.   Res.,   105,   20673–20696,
826   https://doi.org/10.1029/2000JD900282, 2000.

827 Dubovik, O., Holben, B. N., Eck, T. F., Smirnov, A., Kaufman, Y. J., King, M. D.,
828   Tanre, D., and Slutsker, I.: Variability of absorption and optical properties
829   of key aerosol types observed in worldwide locations, J. Atmos. Sci., 59,
830   590–608,
831   https://doi.org/10.1175/1520-0469(2002)059<0590:VOAAOP>2.0.CO;2,
832   2002.

833 Dubovik, O., Sinyuk, A., Lapyonok, T., Holben, B. N., Mishchenko, M., Yang, P.,

834   Eck, T. F., Volten, H., Munoz, O., Veihelmann, B., van der Zande, W. J.,

835   Leon, J. F., Sorokin, M., and Slutsker, I.: Application of spheroid models to

836   account for aerosol particle nonsphericity in remote sensing of desert dust,

837   J. Geophys. Res.-Atmos., 111, D11208,

838   https://doi.org/10.1029/2005JD006619, 2006.

839   Dubuisson, P., Buriez, J. C., and Fouquart, Y.: High spectral resolution solar

840   radiative transfer in absorbing and scattering media, application to the

841   satellite simulation, J. Quant. Spectrosc. Ra., 55, 103–126,

842   https://doi.org/10.1016/0022-4073(95)00134-4, 1996.

843   Eck, T. F., Holben, B. N., Reid, J. S., Dubovik, O., Smirnov, A., O'Neill, N. T.,

844   Slutsker, I., and Kinne, S.: Wavelength dependence of the optical depth of

845   biomass burning, urban, and desert dust aerosols, J. Geophys. Res., 104,

846   31333–31349, https://doi.org/10.1029/1999jd900923, 1999.

847   Eck, T. F., Holben, B. N., Dubovik, O., Smirnov, A., Goloub, P., Chen, H. B.,

848   Chatenet, B., Gomes, L., Zhang, X. Y., Tsay, S. C., Ji, Q., Giles, D., and

849   Slutsker, I.: Columnar aerosol optical properties at AERONET sites in

850   central eastern Asia and aerosol transport to the tropical Mid-Pacific, J.

851   Geophys. Res., 110, D06202, https://doi.org/10.1029/2004JD005274,

852   2005.

853   Estellés, V., Campanelli, M., Utrillas, M. P., Expósito, F., and Martínez-Lozano,

854   J. A.: Comparison of AERONET and SKYRAD4.2 inversion products

855   retrieved from a Cimel CE318 sunphotometer, Atmos. Meas. Tech., 5,

856   569–579, https://doi.org/10.5194/amt-5-569-2012, 2012.

857   Fan, X., Chen, H., Goloub, P., Xia, X., Zhang, W., and Chatenet, B.: Analysis of

858   column-integrated aerosol optical thickness in Beijing from AERONET

859   observations, China Particuol., 4, 330-335, DOI:

860   10.1016/s1672-2515(07)60285-1, 2006.

861   García, O. E., Díaz, J. P., Expósito, F. J., Díaz, A. M., Dubovik, O., Dubuisson,

862   P., Roger, J.-C., Eck, T. F., Sinyuk, A., Derimian, Y., Dutton, E. G., Schafer,

863   J. S., Holben, B. N., and García, C. A.: Validation of AERONET estimates

864   of atmospheric solar fluxes and aerosol radiative forcing by groundbased

865   broadband measurements, J. Geophys. Res., 113, D21207,

866   https://doi.org/10.1029/2008JD010211, 2008.

867 García, O. E., Díaz, J. P., Expósito, F. J., Díaz, A. M., Dubovik, O., and

868   Derimian, Y.: Aerosol radiative forcing: AERONET based estimates,

869   climate Models, InTech, edited by: Druyan, L., ISBN: 978- 953-51-0135-2,

870   2012.

871 Gelencser, A.: Carbonaceous Aerosol, Atmospheric and Oceanographic

872   Sciences Libery., vol. 30. Springer, Netherland., 2004.

873 Giles, D. M., Holben, B. N., Tripathi, S. N., Eck, T. F., Newcomb, W. W.,

874   Slutsker, I., Dickerson, R. R., Thompson, A. M., Mattoo, S., Wang, S.,

875   Singh, R. P., Sinyuk, A., and Schafer, J. S.: Aerosol properties over the

876   Indo-Gangetic Plain: A mesoscale perspective from the TIGERZ

877   experiment, J. Geophys. Res.-Atmos., 116(D18), DOI:

878   10.1029/2011JD015809, 2011.

879 Giles, D. M., Holben, B. N., Eck, T. F., Sinyuk, A., Smirnov, A., Slutsker, I.,

880   Dickerson, R. R., Thompson, A. M., and Schafer, J. S.: An analysis of

881   AERONET aerosol absorption properties and classifications

882   representative of aerosol source regions, J. Geophys. Res.-Atmos., 117,

883   127–135, DOI: 10.1029/2012JD018127, 2012.

884 Gobbi, G. P., Kaufman, Y. J., Koren, I., and Eck, T. F.: Classification of aerosol

885   properties derived from AERONET direct sun data, Atmos. Chem. Phys.,

886   7, 453–458, http://dx.doi.org/10.5194/acp-7-453-2007, 2007

887 Goloub, P., Li, Z., Dubovik, O., Blarel, L., Podvin, T., Jankowiak, I., Lecoq, R.,

888   Deroo, C., Chatenet, B., and Morel, J. P.: PHOTONS/AERONET

889   sunphotometer network overview: description, activities, results,

890   Fourteenth International Symposium on Atmospheric and Ocean

891   Optics/Atmospheric Physics, 6936, 69360V, DOI: 10.1117/12.783171,

892   2007.

893   Haywood, J. M. and Shine, K. P.: The effect of anthropogenic sulfate and soot
894   aerosol on the clear sky planetary radiation budget, Geophys. Res. Lett.,
895   22, 603–606, https://doi.org/10.1029/95GL00075, 1995.

896   He, Q., Li, C., Geng, F., Yang, H., Li, P., Li, T., Liu, D., and Pei, Z.: Aerosol
897   optical properties retrieved from Sun photometer measurements over
898   Shanghai, China, J. Geophys. Res.-Atmos., 117, D16204,
899   https://doi.org/10.1029/2011JD017220, 2012.

900   Holben, B. N., Eck, T. F., Slutsker, I., Tanré, D., Buis, J. P., Setzer, A., Vermote,
901   E., Reagan, J. A., Kaufman, Y. J., Nakajima, T., Lavenu, F., Jankowiak, I.,
902   and Smirnov, A.: AERONET – A Federated Instrument Network and Data
903   Archive for Aerosol Characterization, Remote Sens. Environ., 66, 1–16,
904   https://doi.org/10.1016/S0034-4257(98)00031-5, 1998.

905   Jacobson, M. Z.: A physically based treatment of elemental carbon optics:
906   implications for global direct forcing of aerosols, Geophys. Res. Lett., 27,
907   217–220, DOI: 10.1029/1999gl010968, 2000.

908   Lacis, A. A. and Oinas, V.: A description of the correlated kdistribution method
909   for modeling nongray gaseous absorption, thermal emission, and multiple
910   scattering in vertically inhomogeneous atmospheres, J. Geophys. Res.,
911   96, 9027–9063, DOI: 10.1029/90JD01945, 1991.

912   Lee, K. H., Li, Z., Cribb, M. C., Liu, J., Wang, L., Zheng, Y., Xia, X., Chen, H.,
913   and Li, B.: Aerosol optical depth measurements in eastern China and a
914   new calibration method, J. Geophys. Res., 115, 4038–4044,
915   https://doi.org/10.1029/2009JD012812, 2010.

916   Li, C.C., Mao, J.T., Lau, A.K.H., Chen, J.C., Yuan, Z.B., Liu, X.Y., Zhu, A.H.,
917   and Liu, G.Q.: Characteristics of distribution and seasonal variation of
918   aerosol optical depth in eastern China with MODIS products, Chinese
919   Science Bulletin., 48, 2488-2495, DOI: 10.1360/03wd0224, 2003.

920   Li, Z., Chen, H., Cribb, M., Dickerson, R., Holban, B., Li, C., Lu, D., Luo, Y.,
921   Maring, H., Shi, G., Tsay, S.C., Wang, P., Wang, Y., Xia, X., and Zhao, F.:
922   Overview of the East Asian Studies on tropospheric aerosols, an

923   international regional experiment(EAST-AIRE), J. Geophys. Res., 112,
924   D22S00. http://dx.doi.org/10.1029/2007JD008853, 2007.

925 Li, X., and Zhang, L.: Analysis of aerosol sources and optical properties based
926   on backward trajectory method over SACOL, Acta Physica Sin., 61, 1-9,
927   DOI: 10.7498/aps.61.023402, 2012.

928 Li, Z. Q., Eck, T., Zhang, Y., Zhang, Y. H., Li, D. H., Li, L., Xu, H., Hou, W. Z., Lv,
929   Y., Goloub, P., and Gu, X. F.: Observations of residual submicron fine
930   aerosol particles related to cloud and fog processing during a major
931   pollution event in Beijing, Atmos. Environ., 86, 187–192, DOI:
932   10.1016/j.atmosenv.2013.12.044, 2014.

933 Li, Z., Lau, W. K.-M., Ramanathan, V., Wu, G., Ding, Y., Manoj, M. G., Liu, J.,
934   Qian, Y., Li, J., Zhou, T., Fan, J., Rosenfeld, D., Ming, Y., Wang, Y., Huang,
935   J., Wang, B., Xu, X., Lee, S.- S., Cribb, M., Zhang, F., Yang, X., Takemura,
936   T., Wang, K., Xia, X., Yin, Y., Zhang, H., Guo, J., Zhai, P. M., Sugimoto, N.,
937   Babu, S. S., and Brasseur, G. P.: Aerosol and monsoon climate
938   interactions over Asia, Rev. Geophys., 54, 866–929,
939   https://doi.org/10.1002/2015RG000500, 2016.

940 Li, Z.Q., Xu, H., Li, K. T., Li, D. H., Xie, Y. S., Li, L., Zhang, Y., Gu, X.F., Zhao,
941   W., Tian, Q.J., Deng, R.R., Su, X.L., Huang, B., Qiao, Y.L., Cui, W.Y., Hu,
942   Y., Gong, C.L., Wang, Y.Q., Wang, X.F., Wang, J.P., Du, W.B., Pan, Z.Q.,
943   Li, Z.Z., and Bu, D.: Comprehensive Study of Optical, Physical, Chemical,
944   and Radiative Properties of Total Columnar Atmospheric Aerosols over
945   China: An Overview of Sun–Sky Radiometer Observation Network
946   (SONET) Measurements, Bulletin of the American Meteorological Society.,
947   99(4), 739–755, https://doi.org/10.1175/BAMS-D-17-0133.1, 2018.

948 Luo, Y., Lu, D., Zhou, X., and Li, W.: Analyses on the spatial distribution of
949   aerosol optical depth over china in recent 30 years, Chinese Journal of
950   Atmospheric Sciences., 26, 721-730, DOI: 10.1002/mop.10502, 2002.

951 Mai, B., Deng, X., Xia, X., Che, H., Guo, J., Liu, X., Zhu, J., and Ling, C.:
952   Column-integrated aerosol optical properties of coarse- and fine-mode

particles over the Pearl River Delta region in China, Sci. Total. Environ., 622–623, 481-492, DOI: 10.1016/j.scitotenv.2017.11.348, 2018.

Myhre, G.: Consistency between satellite-derived and modeled estimates of the direct aerosol effect, Science, 325, 187-190, DOI: 10.1126/science.1174461, 2009.

Nakajima, T. and Tanaka, M.: Algorithms for radiative intensity calculations in moderately thick atmospheres using a truncation approximation, J. Quant. Spectrosc. Ra., 40, 51–69, https://doi.org/10.1016/0022-4073(88)90031-3,1988.

Pappalardo, G., Amodeo, A., Apituley, A., Comeron, A., Freudenthaler, V., Linné, H., Ansmann, A., Bösenberg, J., D'Amico, G., Mattis, I., Mona, L., Wandinger, U., Amiridis, V., AladosArboledas, L., Nicolae, D., and Wiegner, M.: EARLINET: towards an advanced sustainable European aerosol lidar network, Atmos. Meas. Tech., 7, 2389–2409, https://doi.org/10.5194/amt- 7-2389-2014, 2014.

Prats, N., Cachorro, V. E., Berjón, A., Toledano, C., and De Frutos, A. M.: Column-integrated aerosol microphysical properties from AERONET Sun photometer over southwestern Spain, Atmos. Chem. Phys., 11, 12535–12547, DOI:10.5194/acp-11- 12535-2011, 2011.

Qin, K., Wang, L.Y., Wu, L.X., Xu, J., Rao, L.L., Letu, H., Shi, T.W., Wang, R.F., 2017. A campaign for investigating aerosol optical properties during winter hazes over Shijiazhuang, China, Atmos. Res., 198, 113-122, https://doi.org/10.1016/j.atmosres.2017.08.018, 2017.

Ramanathan, V., Crutzen, P. J., Kiehl, J. T., and Rosenfeld, D.: Aerosol, climate, and hydrological cycle, Science 294, 2119–2124, https://doi.org/10.1126/science.1064034, 2001.

Remer, L. A., and Kaufman, Y. J.: Dynamic aerosol model: Urban/industrial aerosol, J. Geophys. Res., 103, 13859–13871, https://doi.org/10.1029/98jd00994, 1998.

Roger, J. C., Mallet, M., Dubuisson, P., Cachier, H., Vermote, E., Dubovik, O.,

and Despiau, S.: A synergetic approach for estimating the local direct aerosol forcing: applications to an urban zone during the ESCOMPTE experiment, J. Geophys. Res., 111, D13208, https://doi.org/10.1029/2005JD006361, 2006.

Russell, P. B., Bergstrom, R. W., Shinozuka, Y., Clarke, A. D., DeCarlo, P. F., Jimenez, J. L., Livingston, J. M., Redemann, J., Dubovik, O., and Strawa, A.: Absorption Angstrom Exponent in AERONET and related data as an indicator of aerosol composition, Atmos. Chem. Phys., 10, 1155–1169, https://doi.org/10.5194/acp-10-1155-2010, 2010.

Shettle, E. P., and Fenn, R. W.: Models for the aerosols of the lower atmosphere and the effects of humidity variations on their optical properties. AFCRL Tech. Rep. 79 0214, Air Force Cambridge Research Laboratory, Hanscom Air Force Base, MA, 100 pp, 1979.

Stamnes, K., Tsay, S. C., Wiscombe, W., and Jayaweera, K.: Numerically stable algorithm for discrete-ordinate-method radiative transfer in multiple scattering and emitting layered media, Appl. Optics., 27, 2502–2509, https://doi.org/10.1364/ao.27.002502, 1988.

Su, X. L., Wang, Q., Li, Z. Q., Calvello, M., Esposito, F., Pavese, G., Lin, M. J., Cao, J. J., Zhou, C. Y., Li, D. H., Xu, H.: Regional transport of anthropogenic pollution and dust aerosols in spring to Tianjin — A coastal megacity in China, Sci. Total Environ., 584-585, 381-392, https://doi.org/10.1016/j.scitotenv.2017.01.016, 2017.

Takamura, T., and Nakajima, T.: Overview of SKYNET and its activities, Opt. Pura Apl., 37, 3303–3308, 2004.

Tao, R., Che, H. Z., Chen, Q. L., Wang, Y. Q., Sun, J. Y., Zhang, X. C., Lu, S., Guo, J. P., Wang, H., and Zhang, X.Y.: Development of an integrating sphere calibration method for Cimel sunphotometers in China aerosol remote sensing network, Particuology 13, 88–99. https://doi.org/10.1016/j.partic.2013.04.009, 2014.

Twomey, S. A., Piepgrass, M., and Wolfe, T. L.: An assessment of the impact of

1013   pollution on the global cloud albedo, Tellus, 36B, 356–366,
1014   https://doi.org/10.1111/j.1600-0889.1984.tb00254.x, 1984.

1015   Wan, X., Kang, S.C., Wang, Y.S., Xin, J.Y., Liu, B., Guo, Y.H., Wen, T.X., Zhang,
1016   G.S., and Cong, Z.Y.: Size distribution of carbonaceous aerosols at a
1017   high-altitude site on the central Tibetan Plateau (Nam Co Station, 4730m
1018   a.s.l.), Atmos. Res., 153, 155–164,
1019   https://doi.org/10.1016/j.atmosres.2014.08.008, 2015.

1020   Wang, X., Huang, J.P., Ji, M.X., and Higuchi, K.: Variability of east Asia dust
1021   events and their long-term trend, Atmos. Environ., 42, 3156–3165,
1022   http://dx.doi.org/ 10.1016/j.atmosenv.2007.07.046, 2007.

1023   Wang, L. C., Gong, W., Xia, X. A., Zhu, J., Li, J., and Zhu, Z. M.: Long-term
1024   observations of aerosol optical properties at Wuhan, an urban site in
1025   Central China, Atmos. Environ., 101, 94–102, DOI:
1026   10.1016/j.atmosenv.2014.11.021, 2015.

1027   Wang, P., Che, H. Z., Zhang, X. C., Song, Q. L., Wang, Y. Q., Zhang, Z. H., Dai,
1028   X., and Yu, D. J.: Aerosol optical properties of regional background
1029   atmosphere in Northeast China, Atmos. Environ., 44, 4404–4412, DOI:
1030   10.1016/j.atmosenv.2010.07.043 , 2010.

1031   Wang, Z., Liu, D., Wang, Y., Wang, Z., and Shi, G.: Diurnal aerosol variations
1032   do affect daily averaged radiative forcing under heavy aerosol loading
1033   observed in Hefei, China, Atmos. Meas. Tech., 8, 2901–2907,
1034   https://doi.org/10.5194/amt-8-2901-2015, 2015.

1035   Wehrli, C.: Calibration of filter radiometers for the GAW Aerosol Optical Depth
1036   network at Jungfraujoch and Mauna Loa, in: Proceedings of ARJ
1037   Workshop, SANW Congress, Davos, Switzerland, 70–71, 2002.

1038   Whitey, K. T.: The physical characteristics of sulfur aerosols. Atmos. Environ.,
1039   41(supp-S), 25-49, DOI: 10.1016/j.atmosenv.2007.10.057, 1978.

1040   Wu, Y.F., Zhang, R.J., Pu, Y.F., Zhang, L.M., Ho, K.F., and Fu, C.B.: Aerosol
1041   optical properties observed at a semi-arid rural site in Northeastern China,
1042   Aerosol. Air. Qual. Res., 12,503–514, DOI: 10.4209/aaqr.2011.11.0202 ,

1043   2012.

1044 Xia, X.: A closer looking at dimming and brightening in China during 1961–
1045   2005, Ann. Geophys., 28, 1121–1132, doi:10.5194/angeo-28-1121-2010,
1046   2010.

1047 Xia, X., Chen, H., Goloub, P., Zong, X., Zhang, W., and Wang, P.:
1048   Climatological aspects of aerosol opticalproperties in North China Plain
1049   based on ground and satellite remote-sensing data, J. Quant. Spectrosc.
1050   Ra., 127, 12–23, DOI: 10.1016/j.jqsrt.2013.06.024, 2013.

1051 Xie, C., Nishizawa, T., Sugimoto, N., Matsui, I., and Wang, Z.: Characteristics
1052   of aerosol optical properties in pollution and Asian dust episodes over
1053   Beijing, China. Appl. Opt., 47, 4945-4951, DOI: 10.1364/AO.47.004945,
1054   2008.

1055 Xin, J., Wang Y, Li, Z.Q., Wang, P.C., Hao, W.M., Nordgren, B.L., Wang, S.G.,
1056   Liu, G.R., Wang, L.L., Wen, T.X., Sun, Y., and Hu, B.: Aerosol optical
1057   depth (AOD) and Ångström exponent of aerosols observed by the
1058   Chinese Sun Hazemeter Network from August 2004 to September 2005, J.
1059   Geophys. Res., 112, D05203, DOI: 10.1029/2006JD007075, 2007

1060 Xin, J.Y., Wang, L.L., Wang, Y.S., Li, Z., and Wang, P.: Trends in aerosol
1061   optical properties over the Bohai Rim in Northeast China from 2004 to
1062   2010, Atmos. Environ., 45, 6317–6325, DOI:
1063   10.1016/j.atmosenv.2011.08.052, 2011.

1064 Xin J, Wang Y, Pan Y, Ji, D., Liu, Z., Wen, T.X., Wang, Y.H., Li, X.R., Sun, Y.,
1065   Sun, J., Wang, P.C., Wang, G.H., Wang, X.M., Cong, Z.Y., Song, T., Hu, B.,
1066   Wang, L.L., Tang, G.Q., Gao, W.K., Guo, Y.H., Miao, H.Y., Tian, S.L., and
1067   Wang, L.: The campaign on atmospheric aerosol research network of
1068   China: CARE-China, Bulletin of the American Meteorological Society., 96,
1069   1137-1155, https://doi.org/10.1175/BAMS-D-14-00039.1, 2015.

1070 Yuan, Y., Shuai, Y., Li, X.W., Liu, B., and Tan, H.P.: Using a new aerosol
1071   relative optical thickness concept to identify aerosol particle species,
1072   Atmos. Res., 150, 1–11, DOI: 10.1016/j.atmosres.2014.07.007, 2014.

1073 Zhang, M., Ma, Y., Gong, W., Liu, B., Shi, Y., and Chen, Z.: Aerosol optical
1074   properties and radiative effects: Assessment of urban aerosols in central
1075   China using 10-year observations, Atmos. Environ., 182, 275-285, DOI:
1076   10.1016/j.atmosenv.2018.03.040, 2018

1077 Zhang, R., Jing, J., Tao, J., Hsu, S.-C., Wang, G., Cao, J., Lee, C.S.L., Zhu, L.,
1078   Chen, Z., Zhao, Y., and Shen, Z.: Chemical characterization and source
1079   apportionment of PM2.5 in Beijing: seasonal perspective, Atmos. Chem.
1080   Phys., 13, 7053–7074, http://dx.doi.org/10.5194/acp-13-7053-2013, 2013

1081 Zhao, H., Che, H., Ma, Y., Xia, X., Wang, Y., Wang, P., and Wu, X.: Temporal
1082   variability of the visibility, particulate matter mass concentration and
1083   aerosol optical properties over an urban site in Northeast China, Atmos.
1084   Res., 166, 204–212, DOI: 10.1016/j.atmosres.2015.07.003, 2015.

1085 Zhao H., Che H., Wang Y., Wang H., Ma Y., and Wang Y.: Investigation of the
1086   Optical Properties of Aerosols over the Coastal Region at Dalian,
1087   Northeast China, Atmosphere., 7(8), 103, DOI: 10.3390/atmos7080103,
1088   2016

1089 Zhao, H., Che, H., Xia, X., Wang, Y., Wang, H., Wang, P., Ma, Y., Yang, H., Liu,
1090   Y., Wang, Y., Gui, K., Sun, T., Zheng, Y., and Zhang, X.: Multi-year
1091   ground-based measurements of aerosol optical properties and direct
1092   radiative effect over different surface types in northeastern China, J.
1093   Geophys. Res.-Atmos., **123**, 13,887–13,916,
1094   https://doi.org/10.1029/2018JD029141, 2018

1095 Zhu, J., Che, H., Xia, X., Chen, H. B., Goloub, P., and Zhang, W.:
1096   Column-integrated aerosol optical and physical properties at a regional
1097   background atmosphere in North China Plain, Atmos. Environ., 84, 54–64,
1098   DOI: 10.1016/j.atmosenv.2013.11.019, 2014.

1099 Zhuang, B., Wang, T., Li, S., Liu, J., Talbot, R., Mao, H., Yang, X., Fu, C., Yin,
1100   C., Zhu, J., Che, H., and Zhang, X.: Optical properties and radiative
1101   forcing of urban aerosols in Nanjing over China, Atmos. Environ., 83, 43–
1102   52, DOI: 10.1016/j.atmosenv.2013.10.052, 2014.

Figure captions

Figure 1. Annual spatial distribution of aerosol volume-size distributions at the CARSNET sites

Figure 2. Annual spatial distribution of aerosol optical depth (AOD) at 440 nm at the CARSNET sites

Figure 3. Annual spatial distribution of extinction Ångström exponent (AE) 440-870 nm at the CARSNET sites

Figure 4. Annual spatial distribution of fine mode fraction at the CARSNET sites

Figure 5. Annual spatial distribution of the single scattering albedo (SSA) at 440 nm at the CARSNET sites

Figure 6. Annual spatial distribution of absorption aerosol optical depth (AAOD) at 440 nm at the CARSNET sites

Figure 7. Annual spatial distribution of direct aerosol radiative effect at the bottom of the atmosphere at the CARSNET sites

Figure 8. Annual spatial distribution of direct aerosol radiative effect at the top of the atmosphere at the CARSNET sites

Figure 9. Annual spatial distribution of the aerosol type classification of types I–VII at the CARSNET sites

Table 1 The aerosol type classification based on the optical properties

1124 **Figure 1. Annual spatial distribution of aerosol volume-size distributions**
1125 **at the CARSNET sites**
1126

1127
1128

1129 **Figure 2. Annual spatial distribution of aerosol optical depth (AOD) at 440**

1130 **nm at the CARSNET sites**

1131

1132

1133
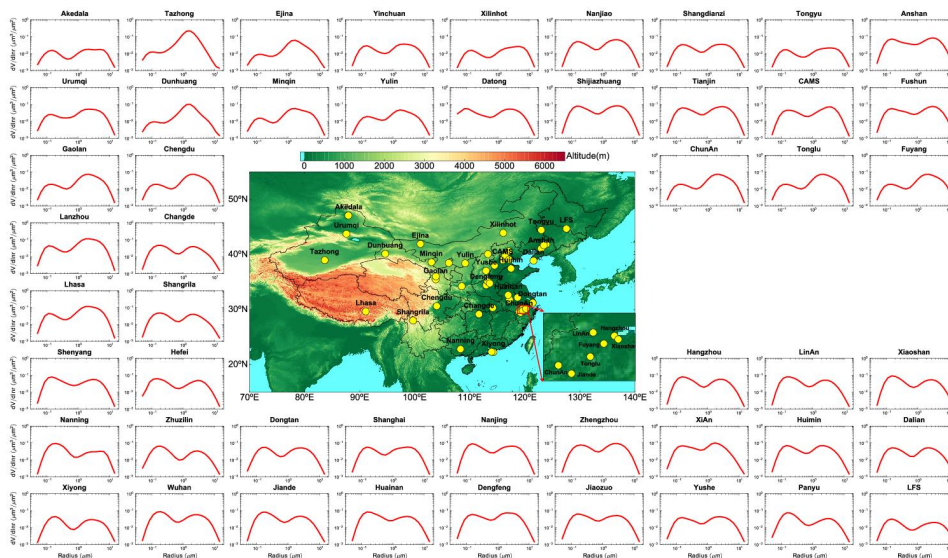
1134 **Figure 3. Annual spatial distribution of extinction Ångström exponent**

1135 **(AE) 440-870 nm at the CARSNET sites**

1136
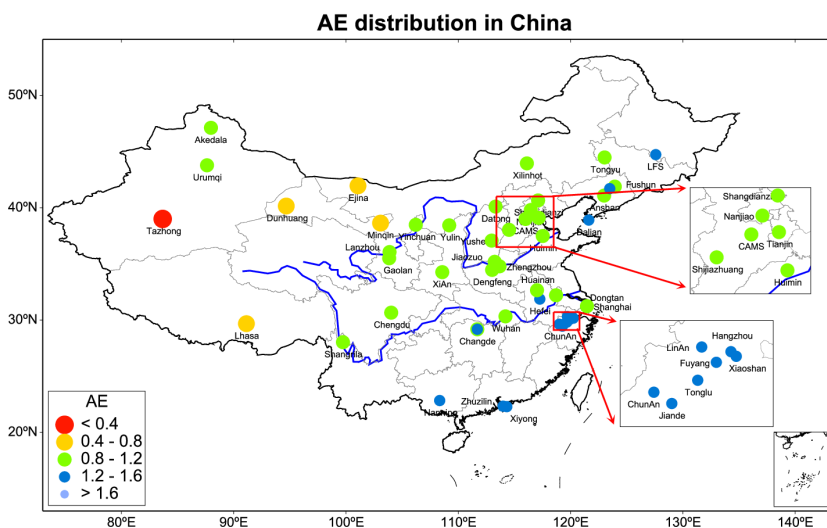
1137
1138

1139 **Figure 4. Annual spatial distribution of fine mode fraction at the**

1140 **CARSNET sites**

1141
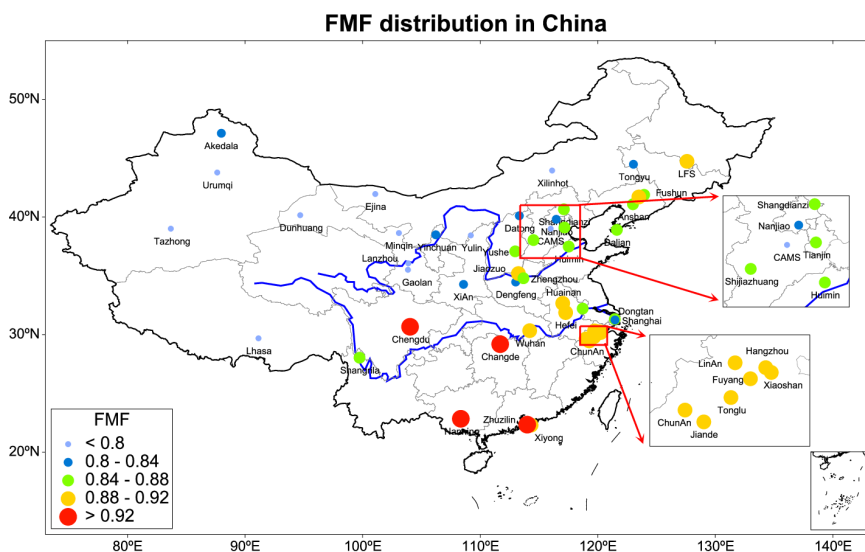
1142
1143

1144 **Figure 5. Annual spatial distribution of the single scattering albedo (SSA)**

1145 **at 440 nm at the CARSNET sites**

1146
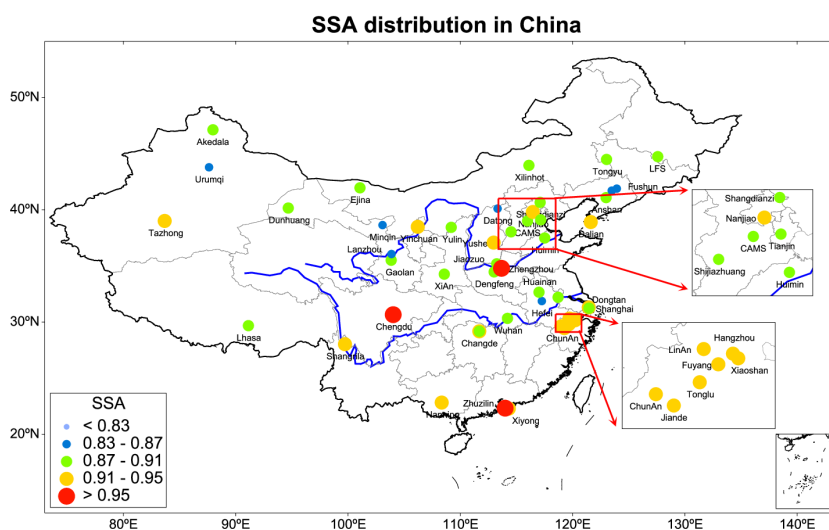
1147

1148

1149

1150

1151 **Figure 6. Annual spatial distribution of absorption aerosol optical depth**
1152 **(AAOD) at 440 nm at the CARSNET sites**
1153
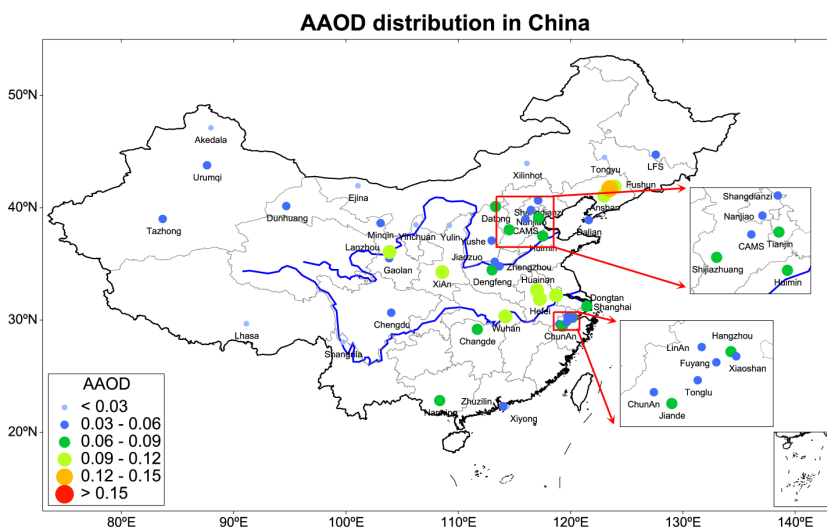
1154
1155

Figure 7. Annual spatial distribution of direct aerosol radiative effect at the bottom of the atmosphere at the CARSNET sites
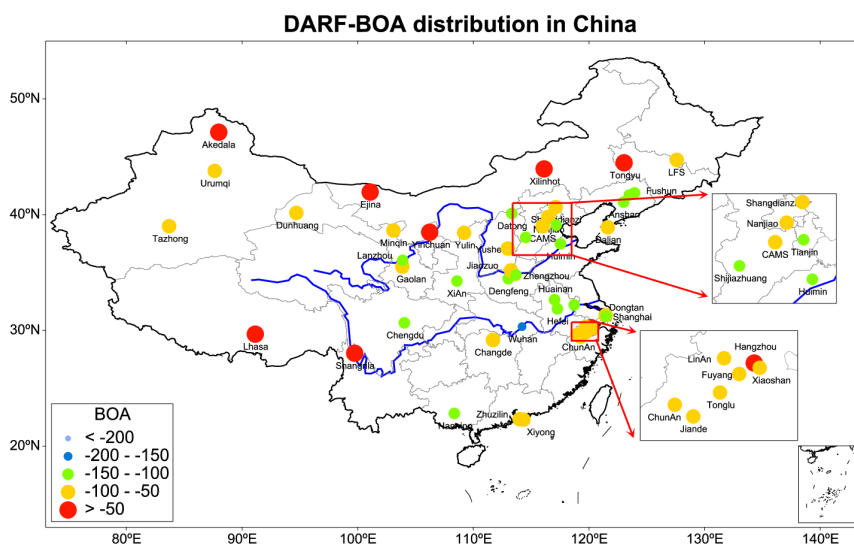
1160   **Figure 8. Annual spatial distribution of direct aerosol radiative effect at**

1161   **the top of the atmosphere at the CARSNET sites**
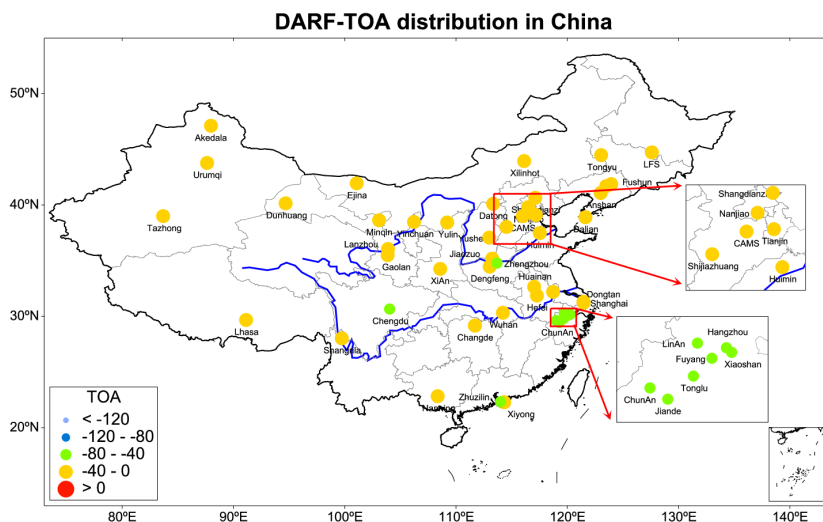
1162

1163

1164 **Figure 9. Annual spatial distribution of the aerosol type classification of**

1165 **types I–VII at the CARSNET sites**

1166
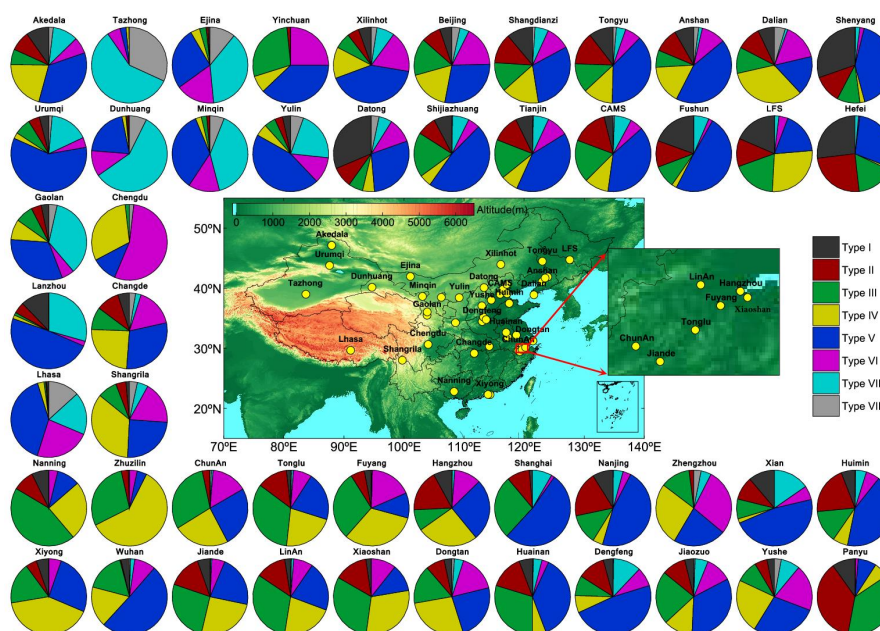
1167
1168

1169   **Table 1. The aerosol type classification based on the optical properties.**

1170

Type	EAE	SSA	absorbing properties and particle size
I	EAE > 1.20	$SSA_{440nm} \leqslant 0.85$	fine-mode particles with highly-absorbing
II	EAE > 1.20	$0.85 \leqslant SSA_{440nm} < 0.90$	fine-mode particles with moderately-absorbing
III	EAE > 1.20	$0.90 \leq SSA_{440nm} < 0.95$	fine-mode particles with slightly-absorbing
IV	EAE > 1.20	$SSA_{440nm} > 0.95$	fine-mode particles with weakly-absorbing
V	$0.60 \leq EAE < 1.20$	$SSA_{440nm} \leq 0.95$	mixed-absorbing particles
VI	$0.60 \leq EAE < 1.20$	$SSA_{440nm} > 0.95$	mixed-slightly absorbing particles
VII	$EAE \leq 0.60$	$SSA_{440nm} \leq 0.95$	coarse mode particles with strongly absorbing (mainly dust)
VIII	$AE \leq 0.60$	$SSA_{440nm} > 0.95$	coarse-mode particles with weakly-absorbing

1171

1172

1173

1174

1175

1176

1177

1178

1179

1180

1181

1182

1183

1184

1185

1186

1187

1188 **Appendix**

1189 **Table 1. Site information for the 50 CARSNET sites used in this study**

1190

No.	Site Name	Long.	Lat.	Alt.	Site information	Obs. Num	Period
					Remote sites (three sites)		
1	Akedala	47.12	87.97	562.0	55 km west of Fuhai county, Xinjiang province, and 250–300 km southeast of Kazakestan.	947	2010-2017
2	Lhasa	29.67	91.13	3663.0	In the center of Lhasa city, Qinghai-Xizang Plateau.	437	2012-2017
3	Shangri-La	28.02	99.73	3583.0	12 km northeast of Shangri-La county, Diqing area, Yunnan province	325	2013-2017
					Arid and semi-arid sites (six sites)		
4	Dunhuang	40.15	94.68	1139.0	1.5 km northeast of Dunhuang city, Gansu province; near Kumutage Desert of China	2030	2012-2017
5	Ejina	41.95	101.07	940.5	West ofIner-Mongolia Province, near Mongolia and Badanjilin desert	1970	2013-2017
6	Minqin	38.63	103.08	1367.0	In Minqin county, east to Tenggeli desert and north to Badanjilin Desert, Gansu Province	481	2013-2017
7	Tazhong	39.00	83.67	1099.4	In the middle of Takilamakan Desert, Xinjiang Province	1279	2013-2017
8	Xilinhot	43.95	116.12	1003.0	5 km southeast of Xilinhot City, near Hunshandake sand-land, Inner-Mongolia Province,	1464	2013-2017
9	Tongyu	44.42	122.87	151.0	In Tonyu city, west of Jilin Province	817	2010-2011
					Rural sites on the Chinese Loess Plateau or nearby (three sites)		
10	Mt.Gaolan	36.00	103.85	2161.6	5 km north of Lanzhou city in Gansu province	769	2015-2016
11	Yulin	38.43	109.20	1135.0	10 km north of Yulin city in Shaanxi province	716	2010-2016
12	Datong	40.10	113.33	1067.3	9 km of Datong City, but within area of rapid urbanization, Shanxi Province	914	2014-2017
					Rural sites in eastern China (15 sites)		
13	Changde	29.17	111.70	565.0	18 km northwest from Changde city, Hunan province.	344	2013-2016
14	Dongtan	31.52	121.96	10.0	In the Chongmin Island, 30km east of Shanghai city	986	2012-2016
15	ChunAn	29.61	119.05	171.4	151 km southwest from Hangzhou city, Zhejiang province.	1286	2011-2015
16	Huimin	37.48	117.53	11.7	100 km Northeast of Jinan City, Shandong Province	2243	2009-2017
17	Lin'an	30.30	119.73	138.6	150 km northeast of Shanghai, and 50 km west of Hangzhou city, Zhejiang province	1834	2011-2015
18	Mt.Longfeng	44.73	127.60	330.5	In Wuchang county, 175 km northeast of Harbin city, Heilongjiang Province	1515	2012-2016
19	Fuyang	30.07	119.95	17.0	44.1 km southwest from Hangzhou city, Zhejiang province.	710	2014-2015
20	Shangdianzi	40.65	117.12	293.0	In Miyun county, 150 km northeast to Beijing city.	1520	2014-2017
21	Yushe	37.07	112.98	1041.5	1.5 km east of Yushe city in Shanxi Province	1479	2013-2017
22	Dengfeng	34.46	113.02	350.0	75 km Southwest of Zhengzhou City, Henan Province	712	2013
23	Huaian	32.65	117.02	52.0	In the central of Hefei City, Anhui Province	794	2014-2015
24	Jiande	29.45	119.28	89.0	In the southwest from Hangzhou city, Zhejiang province.	1550	2011-2015
25	Tonglu	29.80	119.64	46.1	100 km northwest from Hangzhou city, Zhejiang province.	1717	2011-2015
26	Xiaoshan	30.16	120.25	14.0	In the south of Hangzhou city, Zhejiang province.	600	2014-2015
27	Xiyong	22.28	114.33	155.2	In the eastern of Shenzhen city, Guangdong province.	189	2016
					Urban sites (23 sites)		
28	Anshan	41.08	123.00	23.0	In Anshan city, central Liaoning province	193	2009-2013
29	Beijing-Nanjiao	39.80	116.47	31.3	In the southeast Beijing at city margin	1732	2014-2017
30	Beijing-CAMS	39.93	116.32	106.0	Chinese Academy of Meteorological Sciences in Beijing	1113	2012-2018
31	Chengdu	30.65	104.03	496.0	In Chengdu city, Sichuan province.	55	2014-2015
32	Dalian	38.90	121.63	91.5	Southeast coastal city in Liaoning Province	736	2012-2015
33	Fushun	41.88	123.95	80.0	In Fushun city, central Liaoning province.	231	2009-2013
34	Hangzhou	30.23	120.17	42.0	In Hangzhou city, Zhengjiang province.	1663	2011-2015

35	Hefei	31.98	116.38	92.0	In Hefei city, Anhui province.	197	2016
36	Jiaozuo	35.18	113.25	113.0	In the center of Jiaozuo city, Henan province.	981	2016-2017
37	Lanzhou	36.05	103.88	1517.3	In Lanzhou city, Gansu province.	1493	2013-2017
38	Nanjing	32.05	118.77	99.3	In Nanjing city, Jiangsu province	1258	2007-2015
39	Nanning	22.82	108.35	172.0	In Nanning city, Guangxi province	286	2013-2017
40	Panyu	23	113.35	145.0	In district of Guangzhou city, Guangdong Province	436	2012-2016
41	Shanghai	31.22	121.55	14.0	In Pudong district of Shanghai city	144	2016
42	Shenyang	41.77	123.50	60.0	In Shenyang city, central Liaoning province.	541	2009-2013
43	Tianjin	39.10	117.17	3.3	Northern coastal city in North China Plain	1705	2013-2017
44	Urumqi	43.78	87.62	935.0	In Urumuqi city, Xijiang province	1411	2012-2017
45	Xi'an	34.43	108.97	363.0	20 km north of center of Xian city, but within Jing RiverIndustrial District, Shaanxi province	652	2012-2016
46	Yinchuan	38.48	106.22	1111.5	In Yinchuan city, Ningxia province.	124	2017
47	Zhengzhou	34.78	113.68	99.0	In Zhengzhou city, Henan province.	1485	2013-2017
48	Shijiazhuang	38.03	114.53	75.0	In the center of Shijiazhuang city, Hebei province.	1178	2015-2017
49	Wuhan	30.32	114.21	30	In the center of Wuhan city, Hubei province	220	2008
50	Zhuzilin	22.32	114.00	63.0	In the central of Shenzhen city, Guangdong province.	915	2010-2017

1191
1192
1193
1194
1195
1196
1197
1198
1199
1200
1201
1202
1203
1204
1205
1206
1207
1208
1209
1210
1211
1212
1213

1214 **Table 2. Annual data for aerosol microphysical properties, optical and direct radiative parameters**

No.	Site	ᵃReffT	ᵃReffF	ᵃReffC	ᵃVolT	ᵃVolF	ᵃVolC	ᵃAODt	ᵇAlpha	ᵃFMF	ᵃSSAT	ᵃImage	ᵃReal	ᵃAAOD	ᵇBOA	ᵇTOA
							Remote sites (3 sites)									
1	Akedala	0.36	0.14	2.45	0.06	0.02	0.04	0.17	1.13	0.81	0.90	0.0117	1.4540	0.02	-33.65	-0.42
2	Lhasa	0.64	0.13	2.26	0.05	0.01	0.04	0.10	0.77	0.66	0.90	0.0106	1.5541	0.01	-22.13	-5.04
3	Shangri-La	0.39	0.14	2.33	0.03	0.01	0.02	0.10	1.19	0.85	0.93	0.0086	1.4626	0.01	-17.43	-8.93
	Average	0.47	0.14	2.35	0.05	0.01	0.03	0.12	1.03	0.77	0.91	0.0103	1.4902	0.01	-24.40	-4.79
							Arid and semi-arid sites (6 sites)									
4	Dunhuang	0.62	0.14	1.52	0.15	0.02	0.13	0.33	0.48	0.44	0.88	0.0103	1.5491	0.04	-63.61	-8.96
5	Ejina	0.56	0.14	1.78	0.11	0.02	0.09	0.24	0.64	0.52	0.89	0.0116	1.5265	0.03	-47.66	-7.20
6	Minqin	0.56	0.13	1.87	0.13	0.02	0.11	0.30	0.68	0.59	0.86	0.0145	1.5430	0.04	-59.83	-5.01
7	Tazhong	0.71	0.14	1.38	0.30	0.03	0.27	0.60	0.25	0.35	0.92	0.0054	1.5257	0.05	-91.20	-23.49
8	Xilinhot	0.48	0.13	2.45	0.08	0.02	0.05	0.21	1.03	0.78	0.89	0.0139	1.5183	0.02	-37.14	-7.47
9	Tongyu	0.39	0.13	2.36	0.07	0.02	0.05	0.23	1.16	0.82	0.88	0.0179	1.5377	0.03	-39.13	-8.87
	Average	0.55	0.14	1.89	0.14	0.02	0.12	0.32	0.71	0.58	0.89	0.0123	1.5334	0.03	-56.43	-10.17
							Rural sites on the Chinese Loess Plateau or nearby (3 sites)									
10	Mt.Gaolan	0.58	0.14	2.03	0.16	0.03	0.13	0.36	0.81	0.64	0.89	0.0108	1.5154	0.04	-59.36	-20.87
11	Yulin	0.53	0.15	2.05	0.11	0.03	0.08	0.32	0.84	0.72	0.89	0.0122	1.5070	0.03	-56.81	-9.09
12	Datong	0.35	0.13	2.15	0.19	0.09	0.10	0.58	1.15	0.83	0.86	0.0171	1.4905	0.09	-107.86	-13.71
	Average	0.49	0.14	2.08	0.15	0.05	0.10	0.42	0.93	0.73	0.88	0.0134	1.5043	0.05	-74.67	-14.56
							Rural sites in eastern China (15 sites)									
13	Changde	0.32	0.16	2.18	0.14	0.07	0.07	0.58	1.15	0.88	0.93	0.0101	1.4619	0.04	-75.33	-31.44
14	Dongtan	0.37	0.16	2.12	0.17	0.08	0.09	0.62	1.21	0.86	0.93	0.0080	1.4624	0.04	-79.41	-33.18
15	ChunAn	0.30	0.18	2.30	0.19	0.12	0.08	0.81	1.22	0.92	0.94	0.0066	1.4095	0.04	-86.49	-46.48
16	Huimin	0.36	0.15	2.07	0.22	0.10	0.12	0.83	1.14	0.86	0.89	0.0147	1.4852	0.08	-111.58	-25.49

17	Lin'an	0.29	0.17	2.24	0.21	0.12	0.09	0.87	1.29	0.91	0.93	0.0089	1.4172	0.06	-93.09	-41.73
18	Mt.Longfeng	0.28	0.15	2.44	0.08	0.04	0.04	0.34	1.38	0.90	0.89	0.0165	1.4647	0.03	-51.17	-11.34
19	Fuyang	0.29	0.17	2.28	0.21	0.13	0.09	0.89	1.31	0.92	0.94	0.0070	1.4147	0.05	-91.69	-42.29
20	Shangdianzi	0.40	0.15	2.33	0.12	0.05	0.07	0.43	1.17	0.86	0.89	0.0148	1.4840	0.04	-59.99	-20.58
21	Yushe	0.41	0.15	2.18	0.14	0.06	0.08	0.50	1.07	0.84	0.92	0.0090	1.4878	0.03	-66.72	-25.99
22	Dengfeng	0.39	0.15	2.03	0.23	0.09	0.13	0.79	1.02	0.83	0.89	0.0131	1.4782	0.08	-104.78	-35.84
23	Huainan	0.30	0.17	2.25	0.21	0.13	0.08	0.91	1.17	0.92	0.88	0.0166	1.4308	0.10	-129.17	-24.44
24	Jiande	0.29	0.17	2.18	0.20	0.12	0.08	0.84	1.34	0.91	0.92	0.0099	1.4085	0.06	-91.06	-40.07
25	Tonglu	0.29	0.17	2.20	0.20	0.12	0.08	0.83	1.31	0.91	0.93	0.0091	1.4269	0.06	-89.82	-41.28
26	Xiaoshan	0.28	0.17	2.24	0.22	0.13	0.09	0.87	1.35	0.91	0.93	0.0082	1.4134	0.06	-95.23	-40.39
27	Xiyong	0.33	0.16	2.43	0.11	0.06	0.05	0.41	1.32	0.89	0.94	0.0074	1.4072	0.02	-53.18	-25.45
	Average	0.33	0.16	2.23	0.18	0.09	0.08	0.70	1.23	0.89	0.92	0.0107	1.4435	0.05	-85.25	-32.40
Urban sites (23 sites)																
28	Anshan	0.36	0.17	2.24	0.26	0.12	0.14	0.94	1.12	0.86	0.89	0.0158	1.4759	0.10	-117.99	-39.66
29	Beijing-Nanjiao	0.45	0.15	2.33	0.19	0.07	0.12	0.65	1.12	0.84	0.92	0.0100	1.4939	0.05	-82.06	-29.43
30	Beijing-CAMS	0.50	0.16	2.37	0.19	0.07	0.12	0.65	1.12	0.79	0.90	0.0115	1.5108	0.05	-72.66	-29.10
31	Chengdu	0.34	0.21	2.26	0.26	0.16	0.10	1.17	1.12	0.92	0.97	0.0033	1.4116	0.04	-110.42	-52.21
32	Dalian	0.35	0.16	2.24	0.16	0.08	0.09	0.62	1.22	0.87	0.93	0.0095	1.4584	0.04	-75.50	-37.42
33	Fushun	0.38	0.17	2.34	0.22	0.09	0.12	0.80	1.12	0.87	0.84	0.0244	1.4954	0.11	-116.91	-19.59
34	Hangzhou	0.30	0.17	2.21	0.22	0.12	0.10	0.87	1.30	0.90	0.91	0.0109	1.4337	0.07	-31.57	-40.16
35	Hefei	0.29	0.15	2.37	0.18	0.10	0.08	0.69	1.28	0.90	0.85	0.0195	1.4253	0.10	-105.83	-19.22
36	Jiaozuo	0.35	0.16	2.17	0.20	0.10	0.10	0.76	1.14	0.88	0.91	0.0105	1.4722	0.05	-92.29	-39.35
37	Lanzhou	0.54	0.14	2.04	0.28	0.06	0.22	0.66	0.81	0.66	0.83	0.0197	1.5193	0.10	-126.17	-13.81
38	Nanjing	0.33	0.16	2.16	0.25	0.12	0.12	0.94	1.13	0.88	0.88	0.0154	1.4446	0.10	-143.38	-28.29
39	Nanning	0.30	0.18	2.53	0.20	0.13	0.06	0.97	1.36	0.95	0.92	0.0107	1.4272	0.07	-121.92	-33.35
40	Panyu	0.26	0.16	2.29	0.16	0.10	0.06	0.69	1.43	0.93	0.90	0.0137	1.4155	0.07	-96.03	-26.56

41	Shanghai	0.40	0.15	1.93	0.19	0.08	0.11	0.68	1.10	0.84	0.88	0.0142	1.4814	0.07	-106.89	-24.34
42	Shenyang	0.31	0.16	2.23	0.22	0.12	0.10	0.89	1.20	0.90	0.84	0.0253	1.4589	0.14	-144.88	-15.02
43	Tianjin	0.42	0.16	2.26	0.23	0.10	0.13	0.83	1.11	0.86	0.89	0.0134	1.4957	0.07	-108.09	-33.26
44	Urumqi	0.48	0.14	2.14	0.15	0.04	0.10	0.42	0.93	0.75	0.85	0.0192	1.5371	0.05	-70.55	-11.74
45	Xi'an	0.37	0.16	1.85	0.26	0.11	0.15	0.98	0.98	0.82	0.88	0.0150	1.4888	0.10	-132.55	-35.93
46	Yinchuan	0.38	0.14	2.02	0.11	0.04	0.07	0.37	1.12	0.81	0.94	0.0054	1.4930	0.02	-48.67	-21.89
47	Zhengzhou	0.43	0.18	2.22	0.28	0.12	0.16	0.99	1.10	0.86	0.95	0.0045	1.4626	0.04	-101.10	-46.18
48	Shijiazhuang	0.40	0.16	2.28	0.26	0.12	0.14	0.95	1.09	0.87	0.88	0.0154	1.4754	0.09	-125.05	-33.66
49	Wuhan	0.34	0.17	2.22	0.22	0.12	0.10	1.00	1.16	0.91	0.88	0.0196	1.4779	0.11	-171.80	-20.40
50	Zhuzilin	0.27	0.17	2.45	0.15	0.09	0.05	0.66	1.45	0.94	0.96	0.0049	1.4438	0.03	-73.16	-40.65
	Average	0.37	0.16	2.22	0.21	0.10	0.11	0.79	1.15	0.86	0.90	0.0136	1.4695	0.07	-103.28	-30.05

1215 Table 1 (Continued)

1216 [a] Optical parameters at a wavelength of 440 nm.

1217 [b] Angström exponents between 440 and 870 nm.